HHS Public Access

Author manuscript

Hippocampus. Author manuscript; available in PMC 2017 March 01.

Published in final edited form as:

Hippocampus. 2016 March ; 26(3): 341–361. doi:10.1002/hipo.22526.

Mapping the electrophysiological and morphological properties of CA1 pyramidal neurons along the longitudinal hippocampal axis

Malik Ruchi[1,2], **Dougherty Kelly Ann**[1,2,3], **Parikh Komal**[2], **Byrne Connor**[2], and **Johnston Daniel**[2]

[2]Center for Learning and Memory, The University of Texas at Austin, 100 E 24 St, Austin, TX 78712

[3]Department of Biology, Rhodes College, 2000 N Parkway, Memphis, TN 38112

Abstract

Differences in behavioral roles, anatomical connectivity and gene expression patterns in the dorsal, intermediate and ventral regions of the hippocampus are well characterized. Relatively fewer studies have, however, focused on comparing the physiological properties of neurons located at different dorsoventral extents of the hippocampus. Recently we reported that dorsal CA1 neurons are less excitable than ventral neurons. There is little or no information for how neurons in the intermediate hippocampus compare to those from the dorsal and ventral ends. Also, it is not known whether the transition of properties along the dorsoventral axis is gradual or segmented. In this study, we developed a statistical model to predict the dorsoventral position of transverse hippocampal slices. Using current clamp recordings combined with this model, we found that CA1 neurons in dorsal, intermediate and ventral hippocampus have distinct electrophysiological and morphological properties and that the transition in most (but not all) of these properties from the ventral to dorsal end is gradual. Using linear and segmented regression analyses, we found that input resistance and resting membrane potential changed linearly along the V–D axis. Interestingly, the transition in resonance frequency, rebound slope, dendritic branching in stratum radiatum and action potential properties was segmented along the V–D axis. Together, the findings from this study highlight the heterogeneity in CA1 neuronal properties along the entire longitudinal axis of hippocampus.

Keywords

Dorsal hippocampus; ventral hippocampus; intermediate hippocampus; intrinsic excitability; resonance frequency; dendritic branching; firing output

Corresponding Author: Daniel Johnston, Center for Learning and Memory, The University of Texas at Austin, 100 East 24th St, NHB 2.504, C7000, Austin TX, 78712, djohnston@mail.clm.utexas.edu.

[1]these authors contributed equally to this work

Conflicts of Interest: none

Introduction

The rodent hippocampus is widely studied for its unique role in learning and memory. It has become increasingly apparent that hippocampus is not a homogeneous structure, and in fact the hippocampal longitudinal axis (also referred to as dorsoventral or septotemporal axis) is anatomically and functionally segregated (Bannerman et al., 2004; Fanselow and Dong, 2010; Strange et al., 2015). Early studies using targeted lesions and pharmacological blockade of different parts of the longitudinal axis showed that the dorsal two-thirds of the hippocampus is preferentially involved in spatial learning (Moser and Moser, 1998; Moser et al., 1995) and that the ventral one-third part plays an important role in mediating anxiety-like behavior and emotional learning (Kjelstrup et al., 2002; Yoon and Otto, 2007; Zhang et al., 2001). Consistent with the differences in behavioral roles of dorsal (DHC) and ventral hippocampus (VHC), the anatomical connectivity of DHC and VHC is also different. While the dorsal two-thirds of the hippocampus receives visuospatial sensory information from sensory cortices via the medial entorhinal cortex, the VHC on the other hand is highly connected to amygdala, prefrontal cortex (PFC) and hypothalamus (Amaral and Witter, 1989; Dolorfo and Amaral, 1998; Swanson and Cowan, 1977). Additionally, place specific firing fields are discrete and precise in the dorsal end of the hippocampus and the size of the place fields increases from dorsal to ventral end (Jung et al., 1994; Kjelstrup et al., 2008; Poucet et al., 1994). In addition to distinct behavioral roles, diseases of the hippocampus have different effects on the DHC and VHC. Ventral hippocampus and not the dorsal, is considered to be the site of initiation of seizures in temporal lobe epilepsy (Akaikea et al., 2001; Bragdon et al., 1986; Gilbert et al., 1985; Toyoda et al., 2013). In contrast, dorsal CA1 neurons are more prone to damage by ischemia (Ashton et al., 1989).

These functional and neuroanatomical studies argued for distinct dorsal and ventral segments of the hippocampus. Interestingly, a third part of the hippocampal longitudinal axis, called the intermediate hippocampus (IHC) receives DHC like visuospatial inputs and is also connected to the PFC and subcortical areas, such as the amygdala and hypothalamus (Fanselow and Dong, 2010). Owing to this overlapping anatomical connectivity, IHC plays a specific role in rapid place encoding tasks (Bast et al., 2009). Recent gene expression studies in rodents have also provided evidence for distinct molecular boundaries within the longitudinal axis that segregate the hippocampus into dorsal, ventral and intermediate molecular expression zones (Dong et al., 2009; Fanselow and Dong, 2010; O'Reilly et al., 2014; Thompson et al., 2008).

Although the behavioral roles and anatomical connectivity of DHC, VHC and IHC are well characterized, fewer studies have focused on comparing the physiological properties of neurons located at different dorsoventral extents of the hippocampus. Recent *in vitro* electrophysiology studies using slices obtained from dorsal and ventral ends of the hippocampus of adult rats (Dougherty et al., 2012) have shown that CA1 neurons in VHC are intrinsically more excitable than dorsal CA1 neurons. This enhanced excitability of ventral CA1 neurons stems from a more depolarized resting membrane potential (RMP) and higher input resistance (R_{in}) (Dougherty et al., 2012). Also, CA1 neurons from VHC have fewer branches and less dendritic surface area when compared to dorsal CA1 neurons. Interestingly, the differences in electrophysiological properties of dorsal and ventral CA1

neurons are also contributed by differential expression of voltage-gated ion channels, such as hyperpolarization-activated cyclic nucleotide-gated (HCN) channels (Dougherty et al., 2013; Marcelin et al., 2012b). These channels play a crucial role in maintaining the resting properties of CA1 neurons and also significantly affect the integration and transfer of voltage signals along the somatodendritic axis (Magee, 1999; Narayanan and Johnston, 2008; Nolan et al., 2004; Nolan et al., 2007; Vaidya and Johnston, 2013).

Although, the previous slice physiology studies compared the neuronal properties of CA1 neurons located in dorsal and ventral ends of the hippocampus, it is not known whether there are distinct boundaries dividing the dorsal and ventral poles. Also, it is not known whether there is a specialized intermediate part of hippocampus that consists of CA1 neurons that have electrophysiological and morphological properties different from the neurons in the dorsal and ventral poles. An alternative possibility could be that the physiological properties of CA1 neurons gradually change from dorsal to ventral end.

Thus, to test whether transition in the properties of CA1 pyramidal neurons along the longitudinal axis is linear or segmented, we obtained whole-cell current clamp recordings from CA1 neurons in DHC, IHC and VHC slices and quantified hippocampus-wide trends in subthreshold membrane properties, action potential properties, firing output and morphology of CA1 neurons. Using fixed tissue, we developed a coordinate system for the entire longitudinal axis based on measurements within a hippocampal slice. This coordinate system was used to determine the longitudinal position of transverse hippocampal slices *post-hoc*. We show that the CA1 neurons in DHC, IHC and VHC have distinct subthreshold and suprathreshold electrophysiological properties. Also, we observed that the subthreshold membrane properties of CA1 neurons changed linearly along the longitudinal axis. The gradients in morphological properties, I_h sensitive membrane properties and suprathreshold properties were, however, segmented.

Methods

Acute hippocampal slices for electrophysiology

Adult male 1.5–2 month (150–300gms) old Sprague-Dawley rats were used in accordance to the rules and regulations of the University of Texas at Austin Institutional Animal Care and Use Committee. Rats were anaesthetized with a mixture of Ketamine and Xylazine, and transcardially perfused with ice-cold cutting solution containing the following (in mM): 210 sucrose, 1.25 NaH_2PO_4, 25 $NaHCO_3$, 2.5 KCl, 0.5 $CaCl_2$, 7 $MgCl_2$, 7 dextrose, 1.3 ascorbic acid, 3 sodium pyruvate, (bubbled with 95% O_2–5% CO_2, pH ~7.4). Rats were then decapitated, the brains were removed and a cut was made along the midline to separate the two hemispheres.

Four different blocking techniques were used to obtain transverse 350 μm thick slices from dorsal (DHC), intermediate (IHC) and ventral hippocampus (VHC) using a vibrating blade microtome (VT1000A, Leica Microsystems Inc.). DHC and VHC slices were obtained using the same blocking techniques described previously (Dougherty et al., 2012). Briefly, DHC slices were obtained by making a blocking cut at a 45° angle from the coronal plane starting at the posterior end of the forebrain. A second blocking cut was also made at 45° relative to

the coronal plane, but starting from approximately one-third of the total length of the forebrain (from the most anterior point). Brains were mounted on the flat surface created by the first blocking cut. Approximately, 5-6 dorsal slices were obtained from each hippocampus. VHC slices were prepared by laying one hemisphere of the brain on its sagittal surface. A blocking cut was made at 20° relative to the horizontal plane. Tissue was mounted on the flat surface created by the blocking procedure. Approximately three ventral slices were obtained using this technique.

Transverse IHC slices were obtained using two different slicing methods: 1) hemisected brain was placed on its sagittal surface and blocking cut was made approximately 15° to the sagittal plane. Brains were mounted on the flat surface created by this blocking cut and 4–6 slices were obtained; 2) hippocampus was dissected out and parallel blocking cuts were made at one-third and two-thirds extents of the hippocampus. Tissue was mounted on the ventral surface against agar blocks and 5-6 sections were obtained.

Slices obtained using the above-mentioned blocking cuts were transferred to a chamber containing holding saline composed of (in mM): 125 NaCl, 2.5 KCl, 1.25 NaH_2 PO_4, 25 $NaHCO_3$, 2 $CaCl_2$, 2 $MgCl_2$, 12.5 dextrose, 1.3 ascorbic acid, 3 sodium pyruvate (bubbled with 95% O_2 −5% CO_2, pH ∼7.4). Slices were allowed to recover at 37°C for 30 min followed by recovery at room temperature (22–24°C) for 30 minutes. On any given day, two different blocking cuts were used for the two hemispheres. This was done to enhance sampling of electrophysiological recordings from a larger part of the hippocampal long axis for every experimental animal.

Whole-cell patch clamp recordings

Whole-cell current-clamp recordings were obtained from submerged slices perfused in heated (32–34°C) artificial cerebrospinal fluid (aCSF) containing (in mM); 125 NaCl, 3 KCl, 1.25 NaH_2 PO_4, 25 $NaHCO_3$, 2 $CaCl_2$, 1 $MgCl_2$, 12.5 dextrose (bubbled with 95% O_2/5% CO_2, pH ∼7.4). In all experiments 20μM 6,7 dinitroquinoxaline-2, 3-dione (DNQX), 50 μM D, L-2-amino-5 phosphonovaleric acid (D, L-APV) and 2 μM gabazine were added to the aCSF. Neurons were visualized using Zeiss Axioskop microscope fitted with differential interference contrast optics using infrared illumination and an infrared video camera (DAGE-MTI, Michigan city, IN, USA). Pyramidal neurons located in the middle of the proximodistal (CA3–Subiculum) axis of CA1 region, close to stratum radiatum were targeted for recordings. Patch electrodes (4–6 MΩ) were pulled from borosilicate capillary glass of external diameter 1.65 mm (World Precision Instruments) using a Flaming/Brown micropipette puller (model P-97, Sutter Instruments). Electrodes were filled with an internalsolution containing the following (in mm): 120 K-gluconate, 20 KCl, 10 HEPES, 4 NaCl, 7 K_2-phosphocreatine, 0.3 Na-GTP, and 4 Mg-ATP (pH ∼7.3 adjusted with KOH). Neurobiotin (Vector Laboratories) was included (0.1–0.2%) for subsequent histological processing.

Electrophysiology data were recorded using a Dagan BVC-700 amplifier with custom-written acquisition software in the IgorPro environment (Wavemetrics). Signals were low-pass filtered at 3–10 kHz and sampled at 10–40 kHz using an ITC-18 computer interface (InstruTech, Port Washington, NY, USA). Voltages have not been corrected for measured

liquid junction potential (∼8 mV). Upon successful transition to the whole-cell configuration, the neuron was given at least 5 min to stabilize before data were collected. Access resistance and pipette capacitance were appropriately compensated, before each recording. Experiments were terminated if access resistances exceeded 30 MΩ.

Data analysis

Input resistance (R_{in}) was calculated as the slope of the linear fit of the voltage–current plot generated from a family of hyperpolarizing and depolarizing current injections (-50 to +50 pA, steps of 10 pA). The membrane time constant was calculated as the slow component of a double-exponential fit of the average voltage decay in response to a hyperpolarizing current injection (-400 pA, 1 ms). Rebound slope was measured as the slope of the rebound potential amplitude as a function of the steady-state voltage in response to hyperpolarizing current injections. Resonance frequency (f_R) was measured using a sinusoidal current injection of constant amplitude and linearly spanning 0–15 Hz in 15 s (CHIRP15). The impedance amplitude profile (ZAP) was determined by taking the ratio of the fast Fourier transform of the voltage response to the fast Fourier transform of the CHIRP current. Resonance frequency (f_R) was defined as the peak of the ZAP and resonance strength (Q) the ratio of the peak impedance to the impedance at 0.5 Hz.

Firing frequency was calculating by averaging the instantaneous firing frequency of action potentials fired in response to depolarizing current injections. Single action potentials (APs) that occurred 50 ms (±15 ms) after current onset were analyzed for AP threshold, maximum *dV*/*dt* (millivolts per milliseconds), AP amplitude, and AP half-width. Threshold was defined as the voltage at which the value of first derivative of voltage with time exceeded $20 mVms^{-1}$. Action potential amplitude was measured from threshold to peak, with the half-width measured at half this distance. Index of spike-frequency accommodation (SFA) was calculated as the ratio of the last inter-spike interval to the first inter-spike interval for a current injection step that elicited 10-12 spikes (Keshavarzi et al., 2014).

Histological processing and anatomical reconstructions

Slices were fixed with 3% glutaraldehyde in 0.1 M phosphate buffer (pH 7.4) and stored at 4∘C for at least 48 h (up to 3 months). Slices were processed using an avidin-HRP system activated by diaminobenzidine (DAB; Vector Laboratories). DAB-processed slices were mounted in glycerol. Anatomical reconstructions were performed using a compound microscope fitted with a 40× objective and a computer-controlled indexing system running Neurolucida 6.0 imaging software (MBF Bioscience, Williston, VT, USA).

Tissue preparation for construction of hippocampal maps

Serial 300 μm thick transverse hippocampal sections were prepared from nine Sprague-Dawley rats. Rats were anaesthetized and brains were removed using the same methods used for acute slice preparation. Hippocampi were dissected from the brain and were extended using the straightened hippocampal fissure as a guide (Gaarskjaer, 1978). Hippocampi were serially sectioned (ventral to dorsal) in 300 μm increments using a McIlwain tissue chopper. Because the blade was oriented perpendicularly to the hippocampal fissure, all resulting sections were assumed to be transverse. Thick sections (300 μm) were preferred over thinner

sections (100 μm) so that tissue processing and visualization remained comparable to our experimental slices. Sections were immediately fixed with 3% gluteraldehyde, and after 24 hours of fixation, were cleared with glycerol and mounted on glass microscope slides for later visualization. Slice images were obtained using a Zeiss Axio Imager Z2 microscope running AxioVision software (v. 4.8.2; Carl Zeiss, Thornwood, NY).

Anatomical dimensions and scoring guidelines

Images were imported into ImageJ and independently scored by three individuals who were blinded to the longitudinal position of each section. The average of these three measurements was used to build our statistical model. The anatomical dimensions and scoring guidelines were as follows: the transverse length of CA1 (CA1_TL) was determined by tracing the pyramidal cell layer from the CA2 border (noting the transition from large to small, compact pyramids) to the CA1-subiculum border, where the compact pyramidal cell layer disaggregates. The radial length of *stratum lacunosum moleculare* (SLM) in CA1 (CA1_SLM) was determined by drawing a line beginning at the border of *stratum radiatum*, extending across SLM, and ending at the hippocampal fissure. This line originated at approximately 50% of the CA1_TL, and was drawn at an angle perpendicular to the pyramidal cell layer. The transverse length of CA3 (CA3_TL) was determined by tracing the pyramidal cell layer from its origin (near the hilus of the DG) to the distal end of CA2 (i.e., CA2 was included in this measurement). The radial length of CA3 (CA3_RL) was determined by drawing a straight line beginning at the termination of the hippocampal fissure, extending perpendicularly across the pyramidal cell layer, and ending at the alveus. The transverse length of the dentate gyrus (DG_TL) was determined by tracing the granule cell layer from the tip of the infrapyramidal blade to the tip suprapyramidal blade. The tip-to-tip distance (DG_TTD) was determined by drawing a straight line from the tip of the infrapyramidal blade to the tip of the suprapyramidal blade. See Figure 1A and 1B for a visual depiction of these anatomical dimensions and scoring guidelines.

Statistics

Statistical tests and regression analysis were performed using MATLAB and STATA. All plots were made in IGOR Pro. The location of each experimental slice / neuron was mapped along the longitudinal hippocampal axis according to the linear regression model: relative position = $\beta_0 + \beta_1$ (CA1 ratio) + β_2 (DG ratio) + β_3 (CA3 ratio), with the following best-fit estimates: $\beta_0 = -7.23 \pm 0.43$, $\beta_1 = 0.43 \pm 0.02$, $\beta_2 = 0.51 \pm 0.16$, and $\beta_3 = 0.34 \pm 0.086$, Adj-$R^2 = 0.9312$, n = 203 sections (Table 1). Regression using a nested experimental design (i.e., predictors nested within their respective hippocampus) did not significantly improve the predictive capability of the model (data not shown).

Linear and segmented regression analysis of electrophysiological and morphological data was performed using STATA. Data were fitted with linear regressions and segmented regressions with single unknown breakpoints. We also performed segmented regression analysis with unknown multiple break points. For all properties, adding more than one breakpoint did not improve the fit significantly (data not shown). Thus, all segmented regressions shown in this study have one breakpoint. Significant improvement in the fit of the data with segmented regression as compared to linear regression was estimated using the

following criteria: significant increase in adjusted chi-square for the segmented fit, significant breakpoint location and a significant difference between the slopes of the two segments.

Equality of variance for grouped electrophysiology data was tested using Bartlett test and Levene's test. All grouped data distributions were tested for normality using Lilliefors test. The grouped electrophysiology data had unequal variance. Therefore, across group statistical comparisons were made using a non-parametric test, Kolmogorov-Smirnov's test for analysis of variance. This was followed by a pairwise *posthoc* Mann-Whitney U test with a Bonferroni correction.

Results

In this study, we sought to 1) develop a linear coordinate system representing the longitudinal hippocampal axis, 2) map the recorded CA1 neurons onto this coordinate system, and 3) evaluate transition in electrophysiological and morphological properties along the longitudinal axis. Accordingly, serial sections with known longitudinal positions were used to construct a statistical model of the extended hippocampus. The longitudinal positions of the experimental neurons were estimated *post-hoc* using this coordinate system.

Statistical model for mapping slice position in longitudinal axis

Arrays of transverse 300 μm serial sections from nine extended hippocampi served as the raw material for building the linear coordinate system (Figure 1-2). Although the total longitudinal length of the extended hippocampi was approximately 12 mm, only about 10 mm was considered “usable,” as sections from the extreme ventral and dorsal poles contained very few recognizable anatomical landmarks. These sections were not included in subsequent analyses (Slice# 4 & Slice# 38; Fig. 1A). We instead defined the boundaries of the “usable” hippocampus as the first and last sections where a recognizable dentate gyrus was present (i.e., a structure with both supra- and infra-pyramidal blades).

Six anatomical measurements were taken from each remaining section: CA1 transverse length (CA1_TL), CA1 radial length of *stratum lacunosum moleculare* (CA1_SLM), CA3 transverse length (CA3_TL), CA3 radial length (CA3_RL), dentate gyrus transverse length of the granule cell layer (DG_TL), and the tip-to-tip distance between the blades of the dentate gyrus (DG_TTD). Each anatomical dimension was plotted against its known longitudinal coordinate and presented in Figure 1C–E. The anatomical boundaries for each of these measurements are described in the Materials and Methods section and Figure 1B. Because of potential differences in the absolute anatomical dimensions between animals, absolute anatomical measurements were transformed into relative values such that: *CA1 ratio* = CA1_TL/CA1_SLM, *CA3 ratio* = CA3_TL/CA3_RL, and *DG ratio* = DG_TL/DG_TTD. Each section therefore produced three anatomical ratios that were plotted against their known longitudinal position. These particular ratios were chosen as predictors of longitudinal position because they display a linear dependence on relative longitudinal position (n=27 slices; CA1_ratio: $r= 0.98$, $p<0.01$; CA3_ratio: $r=0.88$, $p<0.01$; DG_ratio: $r=0.97$, $p<0.01$; Fig. 1C-E).

Serial arrays obtained from different animals varied by at least the thickness of one slice (300 μm) due to inevitable differences in the starting point for each extended hippocampus. Thus, we normalized the longitudinal position of individual arrays using the index-slice. Index-slice for a given array was defined as the slice where the morphology of the granule cell layer of the dentate gyrus changed from a U-shape to a V-shape (Slice# 21; Fig. 1A). This slice position was marked as the zero point on the longitudinal position axis. Negative longitudinal position values represent the ventral side of the hippocampal array and positive longitudinal position values represent the dorsal side of the hippocampal array (Fig. 2A–F).

Using the anatomical ratios as predictor values (independent variables) and their corresponding relative positions (dependent variable), we performed a multivariate linear regression in order to incorporate these dependencies into a cogent statistical model capable of predicting slice position along the longitudinal axis (Fig. 2G–H). The best-fit estimates of the model coefficients are listed in Table 1. Predictions based on this model indicate that independent transverse slices can be assigned a relative longitudinal position with an accuracy of ± 0.59 mm with 90% confidence, corresponding to approximately 1.2 mm of longitudinal axis.

Mapping experimental slices onto the longitudinal hippocampal coordinate

Whole-cell current-clamp experiments were performed on CA1 pyramidal neurons from positions that spanned nearly 7 mm of the longitudinal hippocampal axis. The corresponding hippocampal slices were generated using four slightly different tissue-blocking techniques, designed to produce arrays of transverse slices from the target regions (top row; Fig. 3A). Because the tissue was blocked with the overlying cortex intact (i.e. hippocampus was not dissected out of the brain) and also due to animal-to-animal variability in blocking cuts, the exact slice position in longitudinal axis was not known during the electrophysiological recordings. After the recordings were obtained, slices were processed for DAB staining. Neurobiotin-filled CA1 neurons that had intact morphology and that were located within the area CA1 (Bottom row; Fig. 3A) were selected for further quantification (n=112 neurons, N=25 rats). The anatomical measurements described above were determined from the selected slices and the regression model was used to predict the longitudinal position of each slice.

The electrophysiological and morphological properties of the recorded CA1 neurons were plotted against their relative longitudinal position. The transition in neuronal properties was evaluated by measurement of the correlation coefficients between the different properties and the position of neurons in the longitudinal axis. Interestingly, for a few properties, the transitions along the longitudinal axis were not linear. To statistically quantify these abrupt transitions, we fitted the electrophysiological properties with segmented regressions. Significant improvement in the regression fits using segmented regressions were ascertained by an increase in adjusted chi-square (R^2) value. In addition to the above-mentioned regression analysis, we binned the longitudinal axis into four segments and statistically compared the difference in physiological properties between all adjacent bins. The longitudinal axis was binned into the following four bins of 1.5 mm length: ventral hippocampus (VHC), intermediate hippocampus closer to ventral end (vIHC), intermediate

hippocampus closer to dorsal end (dIHC) and dorsal hippocampus (DHC) (Fig. 3D). Relative longitudinal position values for the binned data plots were: −2.5 mm corresponding to VHC (n=29), -1 mm corresponding to vIHC (n=23), -0.5 mm corresponding to dIHC (n=34) and 2 mm corresponding to DHC (n=26).

Gradual change in subthreshold membrane properties of CA1 neurons along longitudinal axis

Resting membrane potential (RMP) of CA1 neurons was estimated as the voltage in response to zero current injection. Ventral CA1 neurons had most depolarized RMP and the neurons at the dorsal end had most hyperpolarized RMP. This change in RMP from ventral to dorsal (V–D) end was gradual and RMP of CA1 neurons showed a significant negative correlation with the V–D position (Pearson correlation coefficient (r) = -0.82, P=1e^{-29}; Fig. 3C). The transition in RMP of CA1 neurons along the V–D axis was better fit by a linear regression as the segmented regression did not improve the fit and also no significant breakpoints were observed in transition of RMP along V–D axis (Fig. 3C; Table 2). The difference in RMP across dorsal, intermediate and ventral parts of the hippocampus was also analyzed by binning the V-D axis into four bins of 1.5 mm length (as mentioned above). Resting membrane potential values of CA1 neurons between all adjacent bins were significantly different (VHC: -62.2±0.33 mV, vIHC: -64.8±0.39 mV, dIHC: -67.2±0.29 mV; DHC: -69.6±0.44 mV; Kruskal–Wallis test, P=3.4e^{-17}; Mann-Whitney U test for comparison among groups, P<1e^{-5}; Fig. 3D). It should be noted that the difference in RMP between all adjacent bins was approximately 2 mV.

Similar to the gradient in RMP, the input resistance (R_{in}) of CA1 neurons measured at RMP also decreased from ventral-to-dorsal end of the hippocampus. Statistical analysis showed that R_{in} (at RMP) of CA1 neurons had a strong negative correlation with V–D position (r= -0.85, P= 1e^{-33}; Fig. 4A and Fig. 4C). The transition in R_{in} (at RMP) of CA1 neurons along the V–D axis was adequately described using linear regression as the segmented regression did not improve the fit and no breakpoints were observed (Fig. 4C; Table 2). Furthermore, binning the longitudinal axis showed that differences in R_{in} (at RMP) across all adjacent bins were significant (Kruskal–Wallis test, P=3.4e^{-17}; Fig. 4E). The difference in R_{in} (at RMP) was, however, largest between CA1 neurons in VHC and vIHC (VHC: 93.5±2.6 MΩ, vIHC: 65.6±2.9 MΩ, dIHC: 50.5±2.2 MΩ, DHC: 39.7±1.7 MΩ; Mann-Whitney U test for comparison among groups, P<1e^{-5}).

Since measurement of steady-state R_{in} is dependent on membrane potential of neurons and RMP of CA1 neurons decreases with V–D distance, we measured R_{in} at a common membrane potential (-65mV) (Bottom row; Fig. 4A). Input resistance measured at -65mV was weakly correlated with V–D position (r = -0.31, P= 1e^{-4}; Fig. 4D). Segmented regression of R_{in} (at -65mV) along the V–D axis resulted in a slightly larger adjusted R^2 value when compared with the linear regression (Table 2). The breakpoint location and the difference in slopes of the two segments were, however, not statistically significant (Fig. 4D; Table 2). Analysis of the binned values showed that only the R_{in} (at -65mV) of neurons in the VHC was significantly different from rest of the hippocampal longitudinal axis (VHC: 77±3.1 MΩ, vIHC: 63.8±3.4 MΩ, dIHC: 62.8±3.1 MΩ, DHC: 62.9±3 MΩ; Kruskal–Wallis

test, P=0.004; Mann-Whitney U test for comparison among groups, VHC vs. vIHC: P=0.007; Fig. 4F).

Next, we measured the membrane time constant (measured at RMP) of CA1 neurons from DHC, VHC and IHC slices (Fig. 4B). Our analysis showed that the CA1 neurons in VHC had the longest time constant and the length of the time constant decreased gradually in the ventral-to-dorsal direction (r = -0.31, P= $1e^{-4}$; Fig. 4G). Similar to the gradient in R_{in} (at RMP), the time constant (measured at RMP) of CA1 neurons also changed linearly along the V–D axis (Fig. 4G; Table 2). The time constants of neurons located in VHC and vIHC bins were significantly different (VHC: 32.5±1.4 ms, vIHC: 26.9±1.8 ms, dIHC: 21.6±1.3 ms, DHC: 17.8±1 ms; Kruskal–Wallis test, $P=6.2e^{-10}$; Mann-Whitney U test for comparison among groups, VHC vs. vIHC P<0.01; Fig. 4H).

The analysis of the subthreshold membrane properties identified a significantly larger R_{in} and longer membrane time constant of CA1 neurons located in the VHC as compared to the neurons in dorsal and intermediate parts of the hippocampal longitudinal axis. Importantly, these subthreshold membrane properties changed gradually along this axis.

Change in dendritic morphology along the longitudinal axis

Input resistance and membrane time constant are influenced in part by the complex morphology of pyramidal neurons (Routh et al., 2009). The R_{in} and membrane time constant of CA1 neurons scaled according to the V–D position of the neurons. Thus, we tested whether this gradient in subthreshold properties is matched by differences in morphology of CA1 neurons along the longitudinal position. Although distinct dendritic morphologies of CA1 pyramidal neurons from the DHC and VHC have been reported, less is known about morphologies of the neurons located in intermediate regions of the hippocampus (Dougherty et al., 2012). Here we compared the morphology of neurons along the entire longitudinal axis using a subset of the CA1 neurons from different parts of hippocampal long axis (Fig. 5A; VHC (n=7); vIHC (n=7); dIHC (n=8); DHC (n=7)). The total dendritic length of CA1 pyramidal neurons increased from the ventral to dorsal end of the hippocampus (Fig. 5B). This increase in total dendritic length was fitted best by linear regression (Fig. 5B; Table 3). Interestingly, the radial length of apical dendrites (the path length from the furthest point of the dendrite in SLM to the soma) decreased from the ventral-to-dorsal end (Fig. 5A, 5C). The radial length of CA1 apical dendrites showed a segmented transition along the longitudinal axis as the data were better fitted by segmented regression (Fig. 5C; Table 3).

Another morphological feature that varied with position along the longitudinal axis was dendritic branching. A detailed quantification of the branching pattern of the basal and apical dendrites of CA1 neurons was done using Sholl analysis (Sholl, 1953) (Fig. 5D). The number of intersections of the basal dendrites with the Sholl spheres was lowest for the VHC neurons and increased gradually for the neurons from intermediate and dorsal parts of the hippocampus (Fig. 5E; Table 3). The ventral-to-dorsal change in branching pattern of the apical arbor of CA1 neurons was, however, not gradual (Fig 5F–H). Apical dendrites in the proximal SR and distal SR region of area CA1 located closer to the ventral end had fewer intersections and the number of intersections increased from V–D end. This increase in number of intersections showed an abrupt change along the longitudinal axis. Segmented

regression fits were significantly better than linear fits for the number of intersection in proximal and distal SR region along the longitudinal axis (Fig. 5F; Fig. 5G; Table 3). Interestingly, number of intersections in SLM of area CA1 did not change along the longitudinal axis (Fig. 5H). Overall, the morphological analysis showed that the CA1 neurons closer to the ventral end have longer apical dendrites with fewer dendritic branches in the SR region as compared to the neurons in the intermediate and dorsal parts of the hippocampus.

Changes in resonance and rebound slope along the longitudinal axis

In addition to neuronal morphology, the expression of voltage-gated ion channels has a significant impact on subthreshold membrane properties of CA1 neurons. Recent reports have indicated dorsoventral differences in the expression pattern of HCN channels in CA1 neurons (Dougherty et al., 2013; Marcelin et al., 2012b). A fraction of these HCN channels, which mediate hyperpolarization-induced inward current (I_h), are active near rest and therefore contribute to the R_{in} and RMP of CA1 neurons thereby serving as a key regulator of neuronal excitability (Dougherty et al., 2013; Narayanan and Johnston, 2008). The differences in R_{in} along the longitudinal axis could be in part due to changes in the contribution of I_h. To test this prediction, we used two different current-clamp measurements that provide indirect estimates of amount of I_h in CA1 neurons: resonance frequency, which results from the high-pass filtering properties of I_h (Narayanan and Johnston, 2008); and voltage rebound, which results from the slow deactivation kinetics of I_h (Brager and Johnston, 2007; Magee, 1998). We determined the resonance frequency (f_R) and resonance strength (Q) using the CHIRP15 stimulus injected at RMP and at a common membrane potential (-65mV) (Fig. 6A). Neurons located along the entire longitudinal axis of hippocampus had similar f_R (r=-0.05, *P*=0.57; Fig. 6B; Table 4) and Q (Fig. 6F) when recordings were obtained at their respective resting membrane potentials (VHC: 3.17±0.12 Hz, vIHC: 3.3±0.18 Hz, dIHC: 3.1±0.18 Hz, DHC: 3.08±0.13 Hz; Kruskal–Wallis test, *P*=0.004; Fig. 6C). When measured at a common membrane potential (-65 mV), both f_R (r = -0.47, P< $1e^{-7}$; Fig. 6D) and Q (r=-0.4, *P*<$1e^{-5}$; Fig. 6G) had a significant correlation with V–D distance. Resonance frequency measurements at -65 mV for CA1 neurons fitted better with a segmented regression illustrating a significant breakpoint (Fig. 6D, F; Table 4). Binned data analysis also showed that the f_R (at -65 mV) of the CA1 neurons in the ventral half was significantly larger than the f_R (at -65 mV) of neurons in the dorsal half of the hippocampal long axis (VHC: 3.7±0.17 Hz, vIHC: 3.49±0.17 Hz, dIHC: 2.77±0.11 Hz, DHC: 2.63±0.11 Hz; Kruskal–Wallis test, *P*=$1.6e^{-6}$; Mann-Whitney U test for comparison among groups, vIHC vs. dIHC bin: *P*=0.01; Fig. 6E).

The second indirect measurement that was used to quantify the differences in I_h in CA1 neurons along the longitudinal axis was Rebound Slope (RS). The RS was determined from the voltage responses to a family of hyperpolarizing somatic step current injections starting from either RMP [RS (at RMP)] or a common membrane potential [RS (at -65 mV)] (Fig. 6H). Negative values of rebound slopes are associated with larger I_h and vice versa. We found that the RS (at RMP) decreased in the ventral-to-dorsal direction (r= 0.3, *P*<$1e^{-4}$, Fig. 6I). Stronger correlation with V–D position was observed for RS measured at -65 mV (r=0.54, *P*<$1e^{-10}$; Fig. 6K). Interestingly, for both RS (at RMP) and RS (-65 mV)

measurements from CA1 neurons along the V–D axis followed a segmented regression and showed significant breakpoints (Fig. 6I–K; Table 4). In the binned data comparison, between groups RS values were not different when measured at RMP (VHC: -0.25±0.01, vIHC: -0.21±0.02, dIHC: -0.2±0.01, DHC: -0.2±0.01; Kruskal–Wallis test, P=0.5; Fig. 6J). The same analysis of RS at -65 mV showed significantly larger RS values for the VHC neurons (VHC: -0.3±0.01, vIHC: -0.23±0.02, dIHC: -0.18±0.01, DHC: -0.19±0.02; Kruskal–Wallis test, P=1.6e^{-6}; Mann-Whitney U test for comparison among groups, VHC vs. vIHC: P<0.01; Fig. 6L). These current-clamp measurements suggest that the differences in subthreshold properties along the V–D axis could be partly due to greater I_h in more ventrally located CA1 neurons.

Firing output of CA1 neurons along the longitudinal axis

Differences in subthreshold properties (like RMP and R_{in}) can have a significant influence on firing output of neurons. The firing output is also determined by differences in action potential properties (like threshold, amplitude and half-width). In adult rats, VHC neurons are intrinsically more excitable than DHC neurons (Dougherty et al., 2012). Here we tested whether the increase in firing output is restricted to the neurons located at the ventral end or whether there is a gradual change in firing output along the longitudinal axis. We compared the firing output and single action potential properties of CA1 neurons from DHC, IHC and VHC slices.

Firing output was compared by quantification of the average firing frequency in response to depolarizing somatic current injections (Fig. 7A). The firing frequency in response to two different current intensities (500 pA, 250 pA) was compared. The firing frequency was largest for the VHC neurons and decreased with increasing V–D distance (Fig. 7B–C). The firing frequency of CA1 neurons had a strong negative correlation with V–D position (500 pA current step: r=-0.57, P=3.8e^{-11}; 250 pA current step: r=-0.57, P=2.18e^{-10}). Segmented regression analysis of the firing frequency values of CA1 neurons along the V–D axis showed a significant improvement in the adjusted R^2 and also a significant breakpoint location on the longitudinal axis (Fig. 7B–C; Table 5). The firing frequency of CA1 neurons had a strong negative correlation with V–D position (500 pA current step: r=-0.57, P=3.8e^{-11}; 250 pA current step: r=-0.57, P=2.18e^{-10}). The analysis of binned firing frequency for CA1 neurons showed that the firing frequency was significantly lower in the DHC neurons for both 500 pA current step (VHC: 33.3±1.7 Hz, vIHC: 31.5±1.8 Hz, dIHC: 26.2±1.1 Hz, DHC: 18.4±1.08 Hz; Kruskal–Wallis test, P=4.4^{-11}; Mann-Whitney U test for comparison among groups, vIHC vs. dIHC: P<0.005; dIHC vs. DHC P<1e^{-}5; Fig. 7D) and for 250 pA current injection (VHC: 23±1.3 Hz, vIHC: 20±1.8 Hz, dIHC: 13.4±1.1 Hz, DHC: 5±1.08 Hz; Kruskal–Wallis test, P=7.1^{-13}; Mann-Whitney U test for comparison among groups, vIHC vs. dIHC: P<0.005; dIHC vs. DHC P<1e^{-}5; Fig. 7E). The SFA index of CA1 neurons also showed a strong correlation with V–D position (r=0.53, P=1e^{-9}; Fig. 7F). Unlike the decrease in firing frequency, increase in SFA of CA1 neurons along the V–D axis was gradual because the segmented regression analysis did not show a significant breakpoint (Table 5). In the binned analysis however, VHC neurons showed significantly less accommodation compared to the neurons located elsewhere along the longitudinal axis (VHC: 1.6±0.07, vIHC: 2.1±0.14, dIHC: 2.39±0.11, DHC: 2.56±0.14; Kruskal–Wallis test,

P=3.75^{-7}; Mann-Whitney U test for comparison among groups, VHC vs. vIHC: P<0.005; dIHC vs. DHC: P<0.018; Fig. 7G).

Next, we examined the properties of single action potential properties in CA1 neurons along the longitudinal axis (Fig. 8A). The voltage threshold of single action potentials in CA1 neurons decreased in the V–D direction (r=-0.546, P=5.4e^{-10}; Fig. 8B). The change in AP threshold along the V–D axis was gradual. The AP threshold of CA1 neurons in the VHC was significantly more depolarized as compared to the AP threshold of neurons in the intermediate and dorsal parts of the hippocampus (VHC: -45.8±0.4 mV, vIHC: -48.5±0.5 mV, dIHC: -49.1±0.35 mV, DHC: -49.9±0.43 mV; Kruskal–Wallis test, P=1.8^{-8}; Mann-Whitney U test for comparison among groups, VHC vs. vIHC: P=1e^{-3};Fig. 8C). Another property of the action potentials that varied significantly with the V–D position was the AP half-width. Action potential half-width was positively correlated with V–D position (r=0.34, P=2.1e^{-4}; Fig. 8D). Interestingly, the change in AP half-width of CA1 neurons along the V–D axis fitted better with a segmented regression, thus showing an abrupt change in AP half-width at -1.7 mm of the longitudinal axis. Binned data analysis also showed that CA1 neurons located in the ventral-half of the hippocampus had significantly smaller AP half-widths as compared to the neurons in the dorsal-half of the hippocampus (VHC: 1.03±0.04 ms, vIHC: 1.08±0.05 ms, dIHC: -1.16±0.04 ms, DHC: 1.29±0.05 ms; Kruskal–Wallis test, P=9e^{-4}; Mann-Whitney U test for comparison among groups, vIHC vs. dIHC mm bin: P<0.019; Fig. 8E). A small increase was observed in the AP amplitude of CA1 neurons along the longitudinal axis (r=-0.2, P=0.02; Kruskal-Wallis test, P=0.03; Fig. 8F–G). This increase in AP amplitude also fit better with segmented regression model. Action potential max dV/dt of CA1 neurons was weakly correlated with the longitudinal position (r=-0.23, P=0.015; Kruskal-Wallis test, *P=0.02*; Fig. 8H–I). Similar to AP half-width and AP amplitude, AP max dV/dt values across the longitudinal axis also showed an abrupt change.

Summary

A combination of linear and segmented regression analysis, along with binning of the longitudinal axis showed that subthreshold and suprathreshold electrophysiological properties and also morphological properties of CA1 neurons vary along the longitudinal axis. A key finding of this study is that the passive subthreshold properties (RMP, R_{in} and time constant) change gradually along the longitudinal axis. The total dendritic length and surface area also increase gradually along the V-D end. The change in the radial length of apical dendrites and number of branches in apical dendrites, however, is segmented. The changes in I_h sensitive measurements (at -65 mV) are also segmented along the longitudinal axis. Similar segmentation along the longitudinal axis is observed for firing frequency and AP half-width, amplitude and max. dV/dt. One key observation from the segmented regression analysis is that the breakpoints for most segmented regressions were located at ∼ -2 mm, which is very close to the ventral end of the hippocampus (Table 6). Importantly, we observed segmentation for two properties (RS (at -65 mV) and number of intersections in proximal SR region) near 0.5 mm. Overall, the data in this study provide evidence for both linear and segmented gradients in electrophysiological and morphological properties of CA1 pyramidal neurons along the longitudinal axis. The contribution of these linear and

segmented gradients of CA1 pyramidal neurons properties in governing the neuronal output remains to be explored.

Discussion

The findings in this study highlight the heterogeneity in electrophysiological properties of CA1 neurons across the longitudinal axis of the hippocampus. The differences in intrinsic membrane properties and excitability of CA1 neurons in the dorsal and ventral end of the hippocampus have been described before (Dougherty et al., 2012; Dougherty et al., 2013; Marcelin et al., 2012a). The results in the present study corroborate these previous findings and bridge a significant gap in our understanding of how the neuronal properties transition from one end of the hippocampus to another. Importantly, this is the first study where intrinsic membrane properties of CA1 neurons in dorsal, intermediate and ventral parts of the hippocampus have been compared. The key findings of this study are that the CA1 neurons in DHC, IHC and VHC have distinct electrophysiological and morphological properties and the transition for most of these properties from ventral to dorsal end is gradual. Interestingly, the longitudinal gradients in the dendritic branching, radial length of the apical dendrites, I_h sensitive subthreshold properties and action potential properties were segmented.

Another important aspect of the current study is the development of a coordinate system representing the longitudinal axis of the hippocampus, which can be used to assign dorsoventral position to hippocampal transverse slices. Many laboratories studying the molecular and electrophysiological properties of hippocampal neurons use the hippocampal slices because the cytoarchitecture and synaptic circuits within the hippocampus are preserved in the transverse slice. Hippocampal slice electrophysiology and molecular expression data across laboratories however, do not always match and this could be due to differences in dorsoventral positions of hippocampal slices used in individual studies. The coordinate system for predicting the dorsoventral position developed in our study should provide a useful tool for overcoming this problem. Although, in the present study we generated a slice-scoring system specific for adult rat hippocampi, the same scoring technique can be used to generate slice-scoring maps for rats of different age groups and can also be extended to mouse hippocampus (Supplementary Fig. 1).

Decreased excitability of CA1 neurons in the ventral-to-dorsal direction

The intrinsic membrane properties of neurons and neuronal morphology together shape the input-output dynamics and thereby regulate the firing response of the neuron. The results from this study show that the firing output of the CA1 neurons in response to long depolarizing current injections decreases in the ventral-to-dorsal direction. Interestingly, the V–D gradient in firing frequency is segmented. This decrease in firing in the V–D direction is accompanied by a gradual decrease in R_{in} and hyperpolarized RMP. Since the location of the breakpoint in firing frequency matches with the breakpoint location (-1.7 mm) in the single AP properties, it is plausible that a specific change in AP properties close to the ventral end might underlie the abrupt change in firing output. One proposed mechanism that can underlie changes in AP properties (half-width, amplitude and threshold) in ventral CA1

neurons could be a differential expression of voltage-gated sodium channels (Nav1.2 and Nav1.6) and voltage-gated potassium channels (Kv1 and Kv4 channels) in the somatic and axonal regions of these neurons (Bean, 2007; Colbert and Pan, 2002; Kim et al., 2005; Mitterdorfer and Bean, 2002). It has been shown recently that the expression of M-type (Kv7) potassium channels is higher in dorsal neurons as compared to the ventral CA1 neurons and this dorsoventral difference in M-channel activity underlies the dorsoventral differences in somatic excitability and spike frequency adaptation (Hönigsperger et al., 2015). Although this study quantified M-channel activity at the dorsal and ventral ends, future work will be necessary to test whether the gradient in M-channel activity is gradual or segmented along the longitudinal axis. Interestingly, dorsoventral differences in ion channels that shape the AP properties are not restricted to the soma. A recent study showed that the distal dendrites of ventral CA1 neurons have decreased expression of Kv4.2 channels as compared to the dendrites of dorsal CA1 neurons (Marcelin et al., 2012b). The same study showed reduced transient A-type potassium currents and increased back-propagation of APs in ventral CA1 dendrites. Together, these somatodendritic differences in potassium channels and differences in dendritic morphology along the dorsoventral axis can significantly modulate the neuronal output of CA1 neurons.

One key regulator of membrane excitability in hippocampal neurons is HCN channel mediated I_h. Some of the major functions of I_h are regulation of resting membrane potential, modulation of intrinsic cellular frequency characteristics, and also regulation of membrane resistance (Hutcheon and Yarom, 2013; Magee, 1999; Narayanan and Johnston, 2008; Zemankovics et al., 2010). Recently, two independent studies showed that voltage-dependent activation of I_h and the expression of HCN channel subtypes are different in dorsal and ventral CA1 neurons (Dougherty et al., 2013; Marcelin et al., 2012b). In these studies, current clamp measurements of I_h-dependent membrane f_R and RS were larger in ventral CA1 neurons, indicative of larger I_h in these neurons. In the present study, significant differences in both f_R and RS of CA1 neurons across the longitudinal axis were observed only when the recordings were made at a fixed membrane potential (-65 mV). This was due to the differences in the RMP of the CA1 neurons across the axis. Although, both RS (at -65 mV) and f_R (at -65 mV) were larger for more ventrally located CA1 neurons, the biggest change in f_R was observed for neurons in ventral half of the hippocampus and a large increase in RS was observed for neurons in the ventral one-fourth of the hippocampus. Both f_R and RS are only indicative of levels of I_h in CA1 neurons and future studies aimed at directly measuring I_h will be necessary to understand this discrepancy. Although we observed segmented gradients in f_R and RS, the ventral-to-dorsal gradients in R_{in} and RMP were linear. Because R_{in} and RMP are dependent on both the levels of I_h in CA1 neurons and the morphology, we speculate that the combination of segmented morphological gradient and segmented gradient in I_h might underlie the linear gradient in R_{in} and RMP along the longitudinal axis of the hippocampus. Along with HCN channels, G-protein coupled inwardly rectifying K^+ channels (GIRKs) are also important regulators of subthreshold membrane properties and excitability in CA1 neurons (Ehrengruber et al., 1997). A recent study reported increased levels of GIRKs and their coupling with A1-Adenosine receptors in dorsal CA1 neurons (Kim and Johnston, 2015). Future work aimed at quantification of GIRK channel expression along the longitudinal hippocampal axis will

be crucial to understand the contribution of GIRKs in electrophysiological differences reported in our study.

Functional implications of the heterogeneity in neuronal properties

In this study we found differences in RMP, R_{in}, membrane time constant, resonance frequency, firing output and dendritic branching of individual CA1 neurons in dorsal, intermediate and ventral hippocampus. It is well known that dorsal and intermediate parts of the hippocampus receive visuospatial inputs and the ventral hippocampus is better connected to subcortical areas like the amygdala, hypothalamus and also parts of prefrontal cortex (Amaral and Witter, 1989; Dolorfo and Amaral, 1998). Multiple studies have shown despite the absence of fine spatial inputs to ventral hippocampus, CA1 neurons in the VHC have place fields. The place fields in VHC are, however, larger and less precise than the place fields in dorsal and intermediate hippocampus (Jung et al., 1994; Kjelstrup et al., 2008; Poucet et al., 1994). Although the dorsoventral differences in synaptic inputs and the differences in excitation to inhibition balance (Grigoryan et al., 2012; Maggio and Segal, 2006; Pandis et al., 2006; Papatheodoropoulos et al., 2002) significantly affect the size and shape of place fields, intrinsic membrane parameters transform synaptic inputs as they propagate towards the soma. Therefore, we would reasonably expect that the differences in neuronal excitability observed along the longitudinal axis will exert their own—and presumably significant—influence over place field size and shape (Hussaini et al., 2011; Lee et al., 2012).

Interestingly, recent work from Patel and colleagues showed that the coherence of theta oscillations also decreases from the dorsal-to-ventral direction (Patel et al., 2012). Theta oscillations in dorsal and intermediate parts of hippocampus were more coherent and the decrease in coherence of theta oscillation was most dramatic at the ventral end. Again, these differences in local field potentials between different parts of the dorsoventral axis of the hippocampus could arise due to differences in network properties (Strange et al., 2015) but also by the significant differences in intrinsic membrane properties of CA1 neurons (Vaidya and Johnston, 2013) reported in the current study. It is important to note here that the dorsoventral gradients in intrinsic membrane properties and *in vivo* firing output have also been reported in stellate neurons of medial entorhinal cortex (MEC). Interestingly, the dorsoventral differences in HCN and leak potassium channels and their contribution on synaptic integration in MEC stellate neurons are considered to underlie the dorsoventral differences in grid-cell spacing (Brun et al., 2008; Garden et al.,; Giocomo and Hasselmo, 2009; Giocomo et al., 2007).

The present study was focused on the analysis of gradients in somatic membrane properties, excitability and morphology of CA1 neurons along the longitudinal axis. Future studies aimed at understanding the differences in somato-dendritic integration in CA1 neurons along the longitudinal axis will be necessary to understand the input-output relation of these neurons and also to test whether these differences in intrinsic neuronal properties underlie the behavioral and functional segregation from dorsal to ventral end of the hippocampus.

Supplementary Material

Refer to Web version on PubMed Central for supplementary material.

Acknowledgments

We thank Mohammed Arrafi for technical assistance and Raymond Chitwood for technical advice. We thank Niraj Desai and Department of Statistics at UT Austin for advice and help with statistical methods. We thank Richard Gray, Darrin Brager, Brian Kalmbach, Chung Sub Kim and Elizabeth Arnold for comments on the manuscript and all members of Johnston laboratory for valuable discussions throughout the study.

NIH

Grant number: 9R01NS084473-21 (DJ) and 5F32MH090665 (KAD)

References

Akaikea K, Tanakaa S, Tojoa H, Fukumotoa SI, Imamura BSI, Takigawa M. Kainic acid-induced dorsal and ventral hippocampal seizures in rats. Brain Research. 2001; 900:65–71. [PubMed: 11325347]

Amaral DG, Witter MP. The three-dimensional organization of the hippocampal formation: A review of anatomical data. Neuroscience. 1989; 31:571–591. [PubMed: 2687721]

Ashton D, Van Reempts J, Haseldonckx M, Willems R. Dorsal-ventral gradient in vulnerability of CA1 hippocampus to ischemia: a combined histological and electrophysiological study. Brain Research. 1989; 487:368–372. [PubMed: 2731049]

Bannerman DM, Rawlins JNP, McHugh SB, Deacon RMJ, Yee BK, Bast T, Zhang WN, Pothuizen HHJ, Feldon J. Regional dissociations within the hippocampus—memory and anxiety. Neuroscience & Biobehavioral Reviews. 2004; 28:273–283. [PubMed: 15225971]

Bast T, Wilson IA, Witter MP, Morris RGM. From rapid place learning to behavioral performance: A key role for the intermediate hippocampus. PLoS Biol. 2009; 7:0730–0746.

Bean BP. The action potential in mammalian central neurons. Nat Rev Neurosci. 2007; 8:451–465. [PubMed: 17514198]

Bragdon AC, Taylor DM, Wilson WA. Potassium-induced epileptiform activity in area CA3 varies markedly along the septotemporal axis of the rat hippocampus. Brain Research. 1986; 378:169–173. [PubMed: 3742197]

Brager DH, Johnston D. Plasticity of intrinsic excitability during long-term depression is mediated through mGluR-dependent changes in Ih in hippocampal CA1 pyramidal neurons. The Journal of Neuroscience. 2007; 27:13926–13937. [PubMed: 18094230]

Brun VH, Solstad T, Kjelstrup KB, Fyhn M, Witter MP, Moser EI, Moser MB. Progressive increase in grid scale from dorsal to ventral medial entorhinal cortex. Hippocampus. 2008; 18:1200–1212. [PubMed: 19021257]

Colbert CM, Pan E. Ion channel properties underlying axonal action potential initiation in pyramidal neurons. Nat Neurosci. 2002; 5:533–538. [PubMed: 11992119]

Dolorfo CL, Amaral DG. Entorhinal cortex of the rat: Topographic organization of the cells of origin of the perforant path projection to the dentate gyrus. J Comp Neurol. 1998; 398:25–48. [PubMed: 9703026]

Dong HW, Swanson LW, Chen L, Fanselow MS, Toga AW. Genomic–anatomic evidence for distinct functional domains in hippocampal field CA1. Proceedings of the National Academy of Sciences. 2009; 106:11794–11799.

Dougherty KA, Islam T, Johnston D. Intrinsic excitability of CA1 pyramidal neurones from the rat dorsal and ventral hippocampus. The Journal of Physiology. 2012; 590:5707–5722. [PubMed: 22988138]

Dougherty KA, Nicholson DA, Diaz L, Buss EW, Neuman KM, Chetkovich DM, Johnston D. Differential expression of HCN subunits alters voltage-dependent gating of h-channels in CA1

pyramidal neurons from dorsal and ventral hippocampus. Journal of Neurophysiology. 2013; 109:1940–1953. [PubMed: 23324324]

Ehrengruber MU, Doupnik CA, Xu Y, Garvey J, Jasek MC, Lester HA, Davidson N. Activation of heteromeric G protein-gated inward rectifier K+ channels overexpressed by adenovirus gene transfer inhibits the excitability of hippocampal neurons. Proceedings of the National Academy of Sciences. 1997; 94:7070–7075.

Fanselow MS, Dong HW. Are the Dorsal and Ventral Hippocampus Functionally Distinct Structures? Neuron. 2010; 65:7–19. [PubMed: 20152109]

Gaarskjaer FB. Organization of the mossy fiber system of the rat studied in extended hippocampi. I Terminal area related to number of granule and pyramidal cells. J Comp Neurol. 1978; 178:49–72. [PubMed: 632370]

Garden DLF, Dodson PD, O'Donnell C, White MD, Nolan MF. Tuning of Synaptic Integration in the Medial Entorhinal Cortex to the Organization of Grid Cell Firing Fields. Neuron. 60:875–889. [PubMed: 19081381]

Gilbert M, Racine RJ, Smith GK. Epileptiform burst responses in ventral vs dorsal hippocampal slices. Brain Research. 1985; 361:389–391. [PubMed: 4084805]

Giocomo LM, Hasselmo ME. Knock-Out of HCN1 Subunit Flattens Dorsal-Ventral Frequency Gradient of Medial Entorhinal Neurons in Adult Mice. J Neurosci. 2009; 29:7625–7630. [PubMed: 19515931]

Giocomo LM, Zilli EA, Fransén E, Hasselmo ME. Temporal Frequency of Subthreshold Oscillations Scales with Entorhinal Grid Cell Field Spacing. Science. 2007; 315:1719–1722. [PubMed: 17379810]

Grigoryan G, Korkotian E, Segal M. Selective facilitation of LTP in the ventral hippocampus by calcium stores. Hippocampus. 2012; 22:1635–1644. [PubMed: 22271636]

Hönigsperger C, Marosi M, Murphy R, Storm JF. Dorsoventral differences in Kv7/M-current and its impact on resonance, temporal summation and excitability in rat hippocampal pyramidal cells. The Journal of Physiology. 2015; 593:1551–1580. [PubMed: 25656084]

Hussaini SA, Kempadoo KA, Thuault SJ, Siegelbaum SA, Kandel ER. Increased Size and Stability of CA1 and CA3 Place Fields in HCN1 Knockout Mice. Neuron. 2011; 72:643–653. http://www.sciencedirect.com/science/article/pii/S0896627311007938. [PubMed: 22099465]

Hutcheon B, Yarom Y. Resonance, oscillation and the intrinsic frequency preferences of neurons. TINS. 2013:1–7.

Jung MW, Wiener SI, McNaughton BL. Comparison of spatial firing characteristics of units in dorsal and ventral hippocampus of the rat. The Journal of Neuroscience. 1994; 14:7347–7356. [PubMed: 7996180]

Keshavarzi S, Sullivan RKP, Ianno DJ, Sah P. Functional properties and projections of neurons in the medial amygdala. J Neurosci. 2014; 34:8699–8715. [PubMed: 24966371]

Kim CS, Johnston D. A1 adenosine receptor-mediated GIRK channels contributes to the resting conductance of CA1 neurons in the dorsal hippocampus. Journal of Neurophysiology. 2015 jn.00951.2014.

Kim J, Wei DS, Hoffman DA. Kv4 potassium channel subunits control action potential repolarization and frequency-dependent broadening in rat hippocampal CA1 pyramidal neurones. The Journal of Physiology. 2005; 569:41–57. [PubMed: 16141270]

Kjelstrup KB, Solstad T, Brun VH, Hafting T, Leutgeb S, Witter MP, Moser EI, Moser MB. Finite scale of spatial representation in the hippocampus. Science. 2008; 321:140–143. [PubMed: 18599792]

Kjelstrup KG, Tuvnes FA, Steffenach HA, Murison R, Moser EI, Moser MB. Reduced fear expression after lesions of the ventral hippocampus. Proceedings of the National Academy of Sciences. 2002; 99:10825–10830.

Lee D, Lin BJ, Lee AK. Hippocampal Place Fields Emerge upon Single-Cell Manipulation of Excitability During Behavior. Science. 2012; 337:849–853. [PubMed: 22904011]

Magee JC. Dendritic hyperpolarization-activated currents modify the integrative properties of hippocampal CA1 pyramidal neurons. The Journal of Neuroscience. 1998; 18:7613–7624. [PubMed: 9742133]

Magee JC. Dendritic Ih normalizes temporal summation in hippocampal CA1 neurons. Nature. 1999; 2:508–514.

Maggio N, Segal M. Unique regulation of long term potentiation in the rat ventral hippocampus. Hippocampus. 2006; 17:10–25. [PubMed: 17094146]

Marcelin B, Liu Z, Chen Y, Lewis AS, Becker A, McClelland S, Chetkovich DM, Migliore M, Baram TZ, Esclapez M, Bernard C. Dorsoventral Differences in Intrinsic Properties in Developing CA1 Pyramidal Cells. The Journal of Neuroscience. 2012a; 32:3736–3747. [PubMed: 22423094]

Marcelin B, Lugo JN, Brewster AL, Liu Z, Lewis AS, McClelland S, Chetkovich DM, Baram TZ, Anderson AE, Becker A, Esclapez M, Bernard C. Differential Dorso-ventral Distributions of Kv4.2 and HCN Proteins Confer Distinct Integrative Properties to Hippocampal CA1 Pyramidal Cell Distal Dendrites. Journal of Biological Chemistry. 2012b; 287:17656–17661. [PubMed: 22511771]

Mitterdorfer J, Bean BP. Potassium currents during the action potential of hippocampal CA3 neurons. The Journal of Neuroscience. 2002; 22:10106–10115. [PubMed: 12451111]

Moser MB, Moser EI. Functional differentiation in the hippocampus. Hippocampus. 1998; 8:608–619. [PubMed: 9882018]

Moser MB, Moser EI, Forrest E, Andersen P, Morris RGM. Spatial learning with a minislab in the dorsal hippocampus. Proceedings of the National Academy of Sciences. 1995; 92:9697–9701.

Narayanan R, Johnston D. The h channel mediates location dependence and plasticity of intrinsic phase response in rat hippocampal neurons. The Journal of Neuroscience. 2008; 28:5846–5860. [PubMed: 18509046]

Nolan MF, Dudman JT, Dodson PD, Santoro B. HCN1 channels control resting and active integrative properties of stellate cells from layer II of the entorhinal cortex. The Journal of Neuroscience. 2007; 27:12440–12451. [PubMed: 18003822]

Nolan MF, Malleret GL, Dudman JT, Buhl DL, Santoro B, Gibbs E, Vronskaya S, Buzsáki G, Steven A Siegelbaum, Eric R Kandel, Alexei Morozov. A Behavioral Role for Dendritic Integration: HCN1 Channels Constrain Spatial Memory and Plasticity at Inputs to Distal Dendrites of CA1 Pyramidal Neurons. Cell. 2004; 119:719–732. [PubMed: 15550252]

O'Reilly KC, Flatberg A, Islam S, Olsen L, Kruge I, Witter M. Identification of dorsal–ventral hippocampal differentiation in neonatal rats. Brain Struct Funct. 2014:1–21.

Pandis C, Sotiriou E, Kouvaras E, Asprodini E, Papatheodoropoulos C, Angelatou F. Differential expression of NMDA and AMPA receptor subunits in rat dorsal and ventral hippocampus. Neuroscience. 2006; 140:163–175. http://www.sciencedirect.com/science/article/pii/S0306452206001916. [PubMed: 16542781]

Papatheodoropoulos C, Asprodini E, Nikita I, Koutsona C, Kostopoulos G. Weaker synaptic inhibition in CA1 region of ventral compared to dorsal rat hippocampal slices. Brain Research. 2002; 948:117–121. [PubMed: 12383962]

Patel J, Fujisawa S, Berényi A, Royer S, Buzsáki G. Traveling theta waves along the entire septotemporal axis of the hippocampus. Neuron. 2012; 75:410–417. [PubMed: 22884325]

Poucet B, Thinus-Blanc C, Muller RU. Place cells in the ventral hippocampus of rats. NeuroReport. 1994:2045–2048. [PubMed: 7865741]

Routh BN, Johnston D, Harris K, Chitwood RA. Anatomical and Electrophysiological Comparison of CA1 Pyramidal Neurons of the Rat and Mouse. Journal of Neurophysiology. 2009; 102:2288–2302. [PubMed: 19675296]

Sholl DA. Dendritic organization in the neurons of the visual and motor cortices of the cat. Journal of Anatomy. 1953; 87:387–406. 1. [PubMed: 13117757]

Strange BA, Witter MP, Lein ES, Moser EI. Functional organization of the hippocampal longitudinal axis. Nat Rev Neurosci. 2015; 15:655–669. [PubMed: 25234264]

Swanson LW, Cowan WM. An autoradiographic study of the organization of the efferent connections of the hippocampal formation in the rat. J Comp Neurol. 1977; 172:49–84. [PubMed: 65364]

Thompson CL, Pathak SD, Jeromin A, Ng LL, MacPherson CR, Mortrud MT, Cusick A, Riley ZL, Sunkin SM, Bernard A, Puchalski RB, Gage FH, Jones AR, Bajic VB, Hawrylycz MJ, Lein ES. Genomic anatomy of the hippocampus. Neuron. 2008; 60:1010–1021. [PubMed: 19109908]

Toyoda I, Bower MR, Leyva F, Buckmaster PS. Early Activation of Ventral Hippocampus and Subiculum during Spontaneous Seizures in a Rat Model of Temporal Lobe Epilepsy. The Journal of Neuroscience. 2013; 33:11100–11115. [PubMed: 23825415]

Vaidya SP, Johnston D. Temporal synchrony and gamma-to-theta power conversion in the dendrites of CA1 pyramidal neurons. Nat Neurosci. 2013; 16:1812–1820. [PubMed: 24185428]

Yoon T, Otto T. Differential contributions of dorsal vs. ventral hippocampus to auditory trace fear conditioning. Neurobiology of Learning and Memory. 2007; 87:464–475. [PubMed: 17251041]

Zemankovics R, Káli S, Paulsen O, Freund TF, Hájos N. Differences in subthreshold resonance of hippocampal pyramidal cells and interneurons: the role of h-current and passive membrane characteristics. The Journal of Physiology. 2010; 588:2109–2132. [PubMed: 20421280]

Zhang WN, Bast T, Feldon J. The ventral hippocampus and fear conditioning in rats: different anterograde amnesias of fear after infusion of N-methyl-d-aspartate or its noncompetitive antagonist MK-801 into the ventral hippocampus. Behavioural Brain Research. 2001; 126:159–174. [PubMed: 11704261]

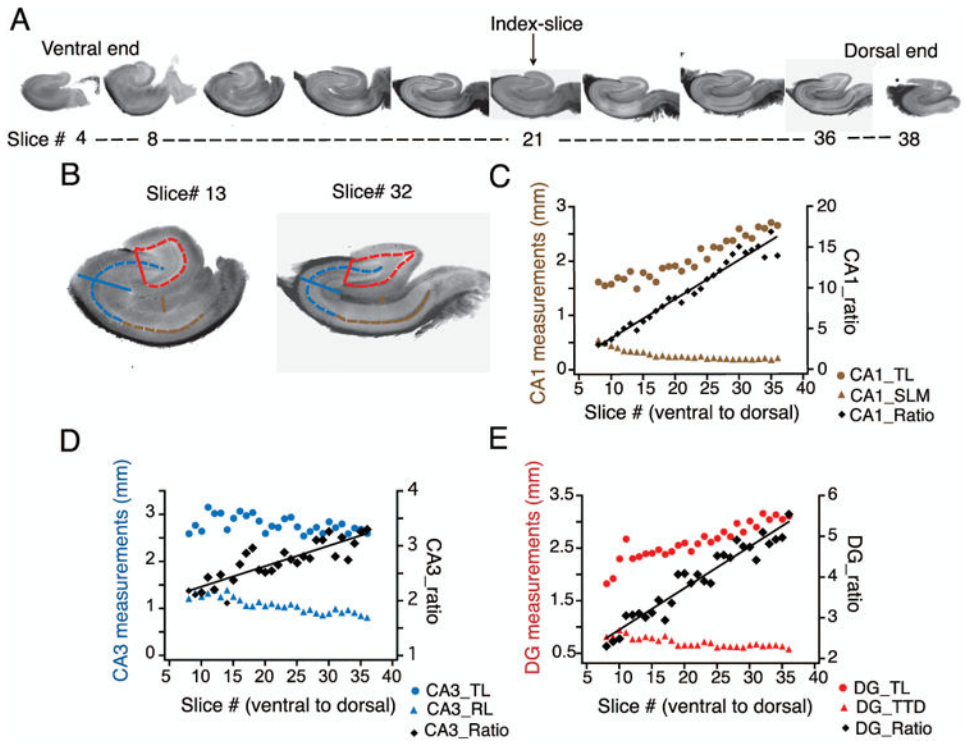

Figure 1. Measurement and quantification of the anatomical predictors of slice position in the longitudinal axis

A) Representative images of hippocampal slices obtained from sectioning an entire hippocampus from the ventral to dorsal (V–D) end. Index-slice represents the slice where the morphology of DG granule cell layer changed from U-Shape to V-shape. **B)** Scheme for measurement of anatomical markers associated with the hippocampal formation depicted using representative slices close to ventral (left, slice # 13) and dorsal end (right, slice # 32): CA1, transverse length (CA1_TL, dashed brown line) and radial length of *stratum lacunosum moleculare* (CA1_SLM, solid brown line); CA3, transverse length (CA3_TL, dashed blue line) and radial length (CA3_RL, solid blue line); DG, transverse length (DG_TL, dashed red line) and tip-to-tip distance (DG_TTD, solid red line). **C-E)** Transverse (circles) and radial (triangles) measurements from CA1 **(C)**, CA3 **(D)** and DG **(E)** are plotted against the slice number (V–D) for one representative hippocampus. The ratios of the transverse-to-radial dimensions (black diamonds) of CA1 **(C)**, CA3 **(D)**, and DG **(E)** are plotted against the slice number. There was a significant linear correlation (tested using *Pearson correlation coefficient*) between the three ratios and slice position (n=27 slices; CA1_ratio: r= 0.98, $p<0.01$; CA3_ratio: r=0.88, $p<0.01$; DG_ratio: r=0.97, $p<0.01$) indicating that these ratios are very good predictors of slice position in the longitudinal axis. Black lines are regression lines.

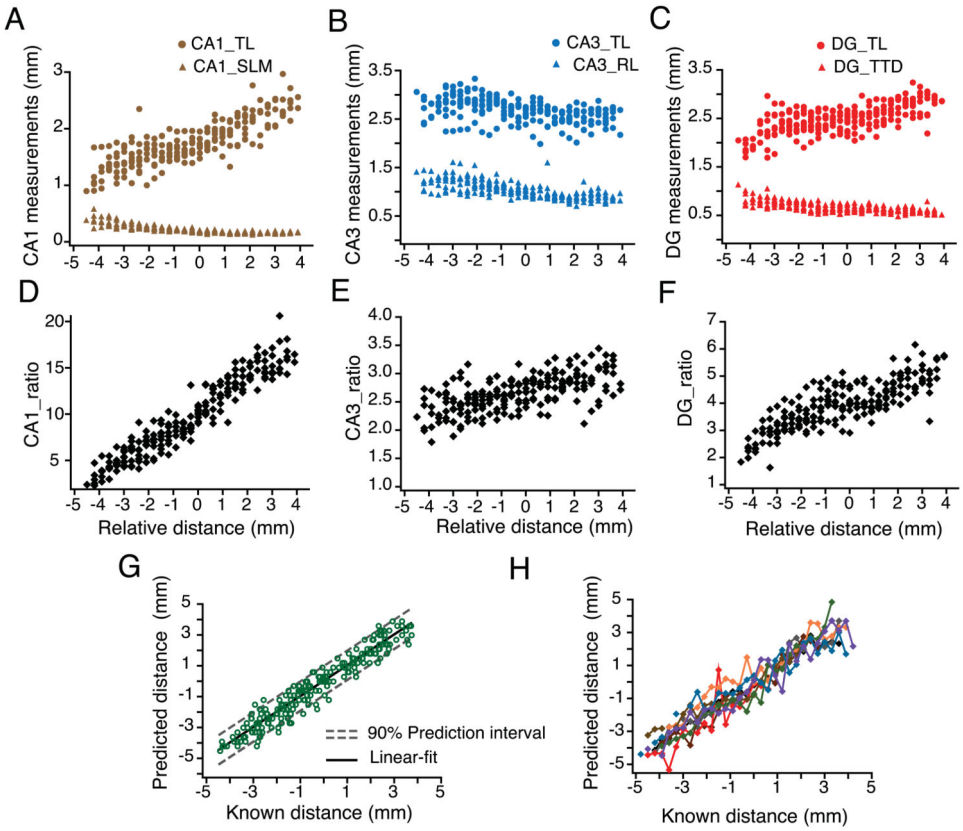

Figure 2. Linear regression model for predicting hippocampal slice position along the longitudinal axis

A-C) Trends in transverse (circles) and radial (triangles) measurements of CA1 (A), CA3 (B) and DG (C) compiled for all hippocampi (n=9) plotted against the relative ventral to dorsal distance (V–D). The relative distances of each set of hippocampal slices were aligned using the index-slice (represented as zero). **D-F)** The ratios of the transverse-to-radial dimensions of the CA1 **(D)**, CA3 **(E)**, and DG **(F)** for all hippocampi were plotted against their relative longitudinal distance from the index-slice. **G)** CA1, CA3 and DG ratios from **(D-F)** were used to build a linear regression model according to the following equation: relative distance = $\beta_0 + \beta_1$ (CA1 ratio) + β_2 (DG ratio) + β_3 (CA3 ratio). The predicted position of each hippocampal slice is plotted against its known distance (open green circles), resulting in a linear relationship (black line represents the linear fit). Dashed grey lines are best-fit lines to the upper and lower bounds of the prediction interval for each point with 90% confidence. **H)** Data in **(G)** are replotted and color-coded to depict predicted and known position for slices from individual hippocampal arrays.

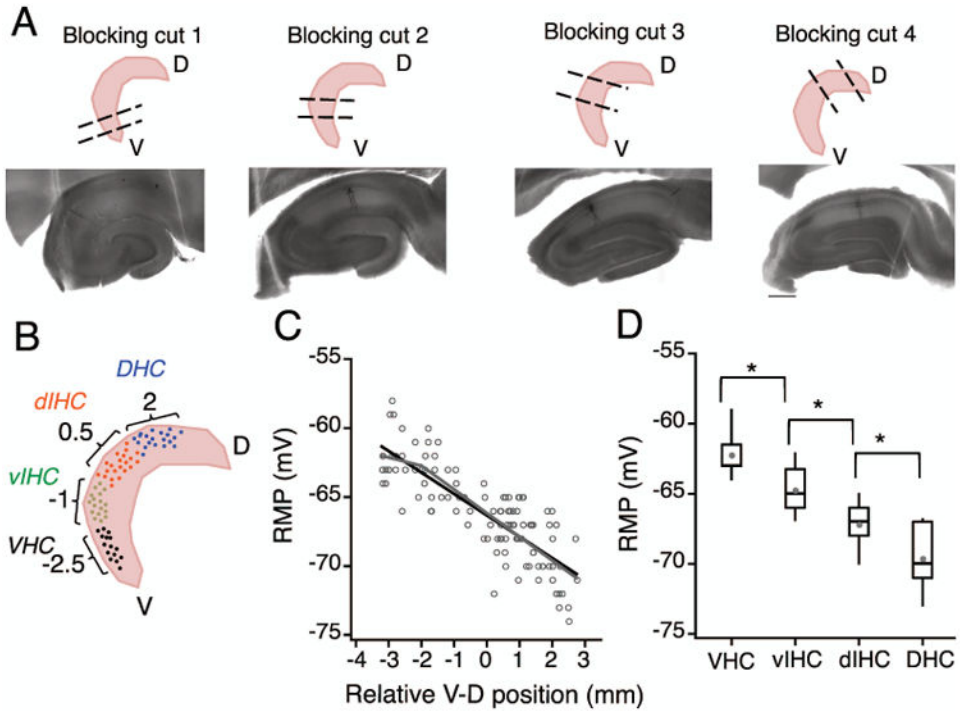

Figure 3. Using the coordinate system to predict longitudinal position of recorded slices

A) Top row: Schematic representation of the four blocking angles used to obtain transverse sections from the ventral (blocking cut one), intermediate (blocking cuts two and three) and dorsal parts of the hippocampus (blocking cut four). Bottom row: Neurobiotin filled CA1 neurons in representative hippocampal sections obtained using the four different blocking angles. Note that the anatomical features of CA1, CA3 and DG are very different in the four example sections. **B)** Schematic to illustrate binning of recorded CA1 neurons into four groups based on the predicted longitudinal position (calculated using the linear regression model) **C)** Plot showing the resting membrane potential (RMP) of CA1 neurons against the relative ventral to dorsal (V-D) position of individual neurons. Note that the resting membrane potential (RMP) of CA1 pyramidal neurons was more depolarized at the ventral end and it decreased linearly along the longitudinal axis. There was a significant negative correlation (black regression line) between the RMP of CA1 neurons and the location of neurons along the longitudinal axis (r = -0.82, $P<1e^{-29}$). Grey lines are the segmented regression fits of RMP values. **D)** The effect of V-D position on change in RMP of CA1 neurons was analyzed by binning the longitudinal axis into four groups (bin-size: 1.5 mm). Data are presented as whisker box plots displaying median, lower (25%) and upper (75%) quartiles, and whiskers representing 10% and 90% range of the data points. Grey filled circles represent the mean RMP value for every bin. RMP was most depolarized for neurons in VHC and decreased in all the subsequent bins. Resting membrane potential of neurons between all adjacent bins was significantly different (Kruskal-Wallis test, $P=3.4e^{-17}$; Mann-Whitney U test for comparison among groups, $^{**}P<1e^{-5}$).

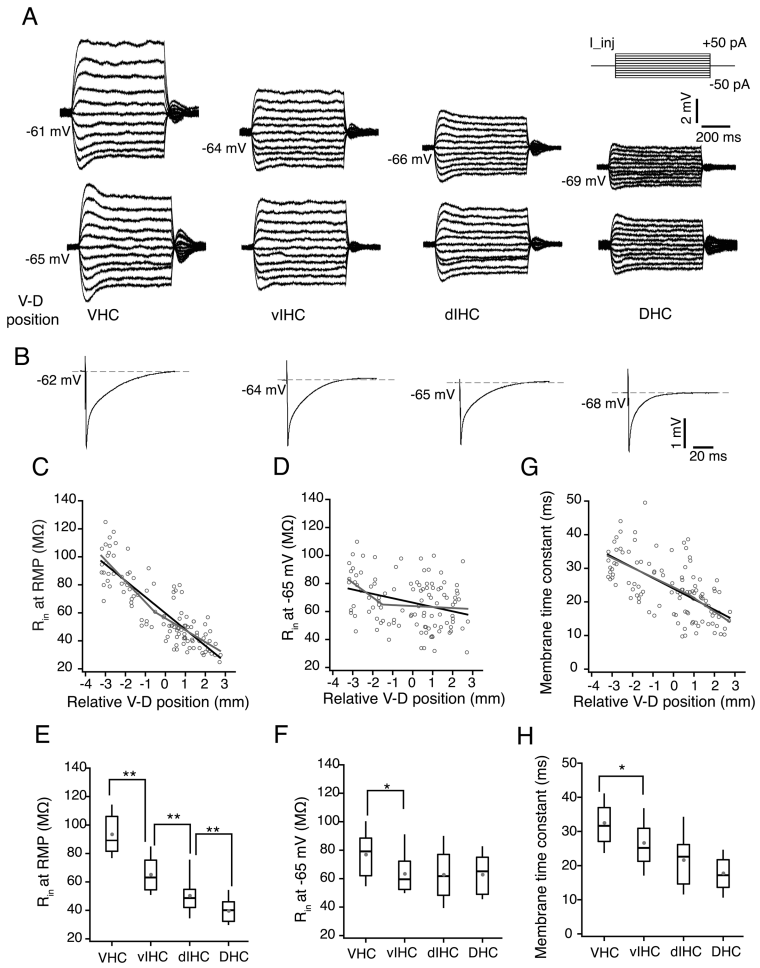

Figure 4. Subthreshold membrane properties of CA1 neurons along the longitudinal axis of hippocampus

A) Representative voltage responses to 800 ms depolarizing and hyperpolarizing current injections (-50 to +50 pA, steps of 10 pA; top right schematic) during somatic whole-cell current clamp recordings from representative CA1 neurons from VHC, vIHC, dIHC and DHC. Top row, voltage responses recorded at the resting membrane potentials (RMP) of individual neurons. The numbers on the left side of the traces indicate the RMP. Note that the RMP of four representative neurons were very different. Bottom row, voltage responses from the same neurons recorded at common membrane potential (-65 mV). **B)** Representative voltage responses to 1 ms long hyperpolarizing current injection (-400pA) from representative CA1 neurons from four bins of longitudinal axis. **C-D and G)** Scatter plots for input resistance (R_{in} at RMP) **(C)**, R_{in} measured at -65 mV **(D)** and membrane time constant measured at RMP **(G)** of CA1 neurons against their relative ventral to dorsal (V–D) position. Black lines are the linear fits. Grey lines are the segmented fits. Significant negative correlation was observed between the R_{in} (at RMP) of CA1 neurons (r = -0.85, $P < 1e^{-33}$) and the location of the neurons in V–D axis **(C)**. Input resistance of CA1 neurons measured at -65 mV also decreased from ventral to dorsal end **(D)** but the correlation was weaker than the correlation of R_{in} at RMP (r = -0.31, $P < 1e^{-4}$). There was a significant negative correlation between the time constant **(G)** and V–D position (r = -0.31, $P = 1e^{-4}$). **E-**

F and H) R_{in} (at RMP) **(E)**, R_{in} (at -65 mV) **(F)** and membrane time constant (at RMP) (H) for binned V-D positions are shown as whisker box plots displaying median. Grey filled circles are mean values. The R_{in} (at RMP) values between all adjacent bins were significantly different (Kruskal-Wallis test, $P=3.4e^{-17}$; Mann-Whitney U test for comparison among groups, $^{**}P<1e^{-5}$). R_{in} (at -65mV) was significantly different for the neurons located in VHC as compared to neurons located elsewhere in the longitudinal axis (Kruskal-Wallis test, $P=0.004$; Mann-Whitney U test for comparison among groups, $^{*}P=0.007$). Membrane time constant (at RMP) was also significantly different for neurons in VHC (Kruskal-Wallis test, $P=6.2e^{-10}$; Mann-Whitney U test for comparison among groups, $^{*}P<0.01$).

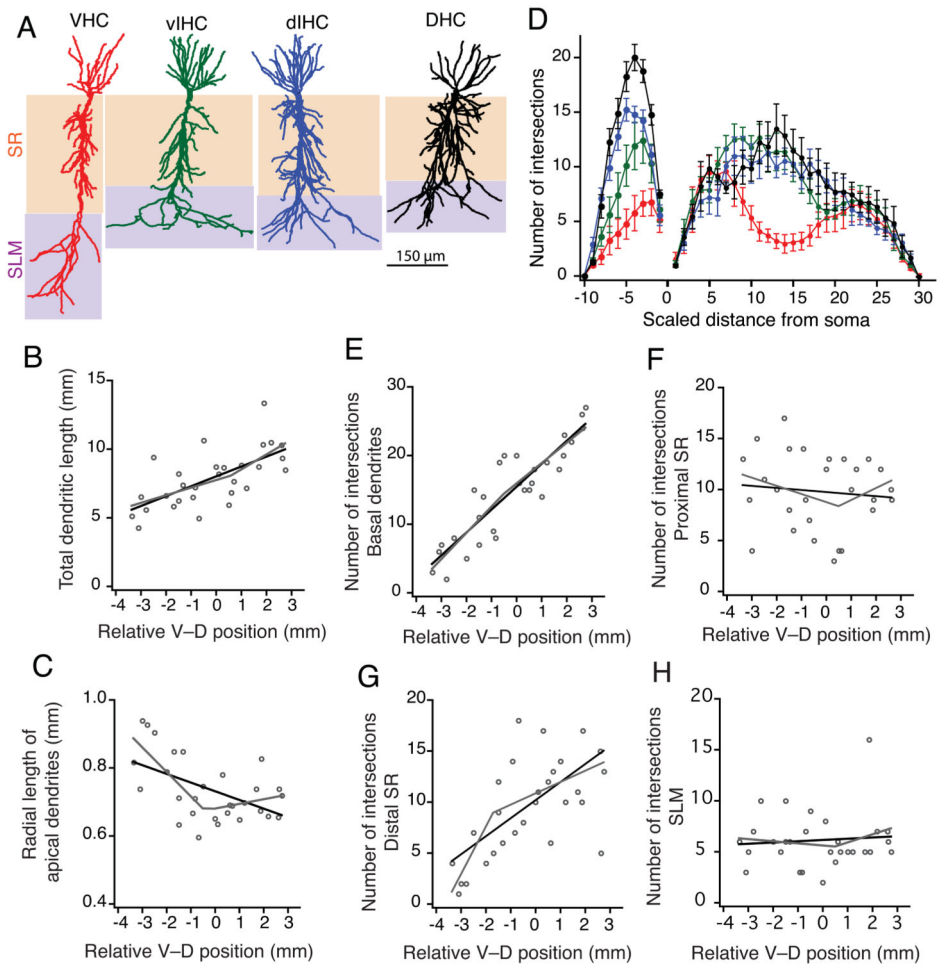

Figure 5. Morphological properties of CA1 neurons along the longitudinal axis

A) Morphological reconstructions of representative CA1 neurons from four regions of the longitudinal axis. Layer stratum radiatum (SR) is shaded brown. Layer stratum lacunosum-moleculare (SLM) is shaded purple. **B)** Total dendritic length of CA1 dendrites increased linearly from ventral to dorsal end. This increase was gradual (linear fit shown as black line) as the segmented regression was not significant (segmented fit shown as grey line). **C)** Radial length of the apical dendrites decreased from ventral to dorsal end. Change in radial apical length was abrupt as the segmented regression fit (grey line) was significantly better than the linear fit (black line). **D)** Number of intersections with Sholl spheres is plotted against dendritic distances. Distance between Sholl radii was adjusted so that 30 and 10 spheres described the apical and basal trees, respectively. Basal and apical dendrites of CA1 neurons from VHC had significantly fewer intersections with Sholl spheres than neurons from other regions along the longitudinal axis (Two-way ANOVA, $p=7.6e^{-10}$). **E-H)** Scatter plots showing the V–D change in number of intersections with Sholl spheres for basal dendrites **(E)**, in proximal SR region **(F)**, in distal SR region **(G)**, and in SLM **(H)**. Black lines are linear fits and grey lines are segmented fits. Number of intersections in basal dendrites increased gradually from ventral to dorsal end. The increase in number of

intersections in proximal and distal SR was segmented. No change in number of intersections in SLM along the longitudinal axis.

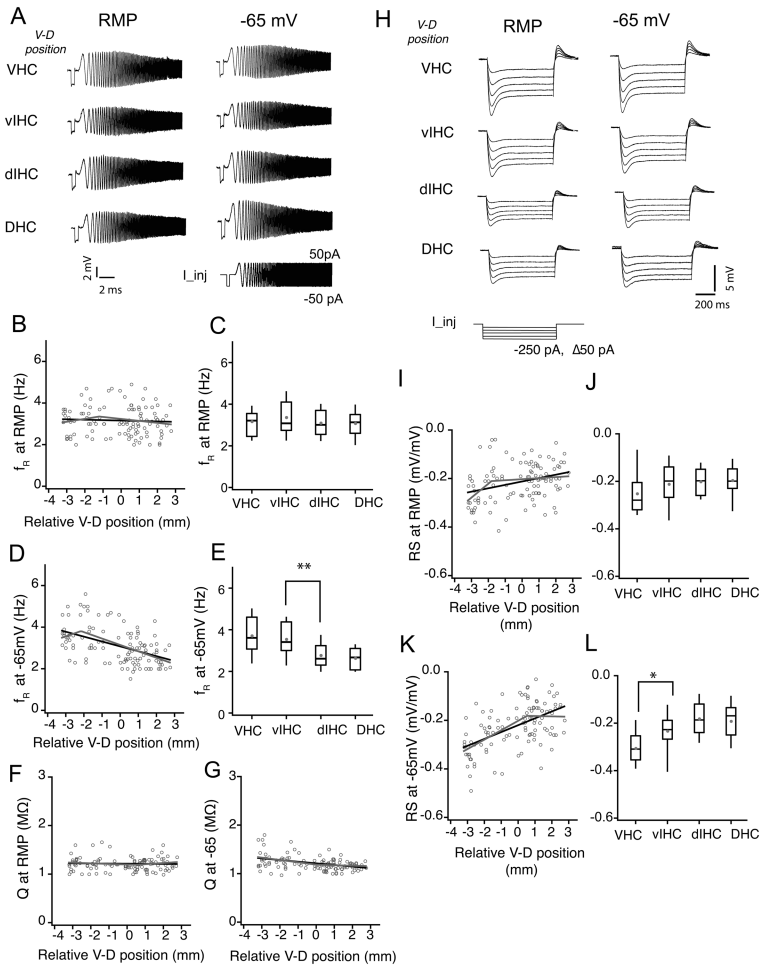

Figure 6. I_h sensitive subthreshold membrane properties of CA1 neurons along the longitudinal axis of hippocampus

A) Representative voltage traces illustrating the membrane resonance in response to a chirp stimulus (0-15 Hz, 15 s) during somatic whole-cell current clamp recordings from example CA1 neurons from four bins of the ventral to dorsal (V–D) axis. **B, D, F and G)** Scatter plots for resonance frequency (f_R) measured at RMP **(B)**, f_R measured at -65 mV **(D)** and resonance amplitude (Q) measured at RMP **(F)** and measured at -65 mV **(G)** of CA1 neurons against their relative V–D position. There was no correlation between the f_R **(B)** and Q **(F)** measured at RMP (f_R: r=-0.05, *P=0.57*; Q: r=-0.03, *P=0.73*). When measured at -65 mV, f_R **(D)** showed a significant negative correlation with V-D distance (black line is linear fit; grey line is segmented fit) and Q **(G)** also showed a significant negative correlation (r=-0.4, $P<1e^{-5}$). **C, E)** Resonance frequency of CA1 neurons measured at RMP and -65 mV was plotted as whisker and box plots showing the median values. Grey circles illustrate the mean values. f_R (at RMP) was similar for neurons across the longitudinal axis (C) (Kruskal-Wallis test, *P=0.004*). f_R measured at -65 mV (E) was significantly different for CA1 neurons from VHC and vIHC (Kruskal-Wallis test, $P=1.6e^{-6}$; Mann-Whitney U test for comparison among groups, $^{**}P<0.001$). **H)** Representative voltages responses to hyperpolarizing current injections during somatic whole-cell current clamp recordings from example CA1 neurons from four bins of the V–D axis. **I, K)** Rebound slope (RS) measured

at RMP **(I)** and at -65 mV **(K)** for CA1 neurons plotted against the V–D position of individual neurons. Note that the RS measured at -65 mV had a stronger positive correlation with V-D position (r=0.54, $P<1e^{-10}$) as compared to the RS measured at RMP (r= 0.3, $P<1e^{-4}$). **J, L)** RS data are plotted as whisker and box plots showing median values. Grey circles are mean values. RS measured at -65 mV **(L)** for the neurons in VHC was significantly different from the neurons in the rest of the longitudinal axis (Kruskal-Wallis test, $P=1.6e^{-6}$; Mann-Whitney U test for comparison among groups, $*P<0.01$)

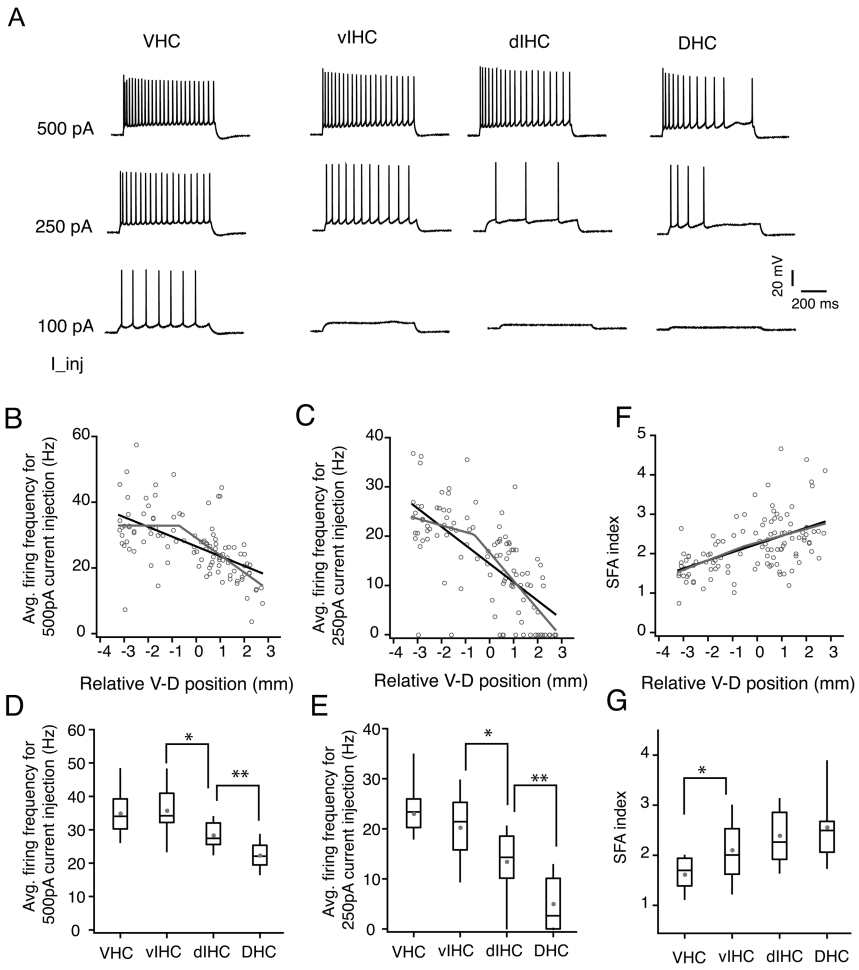

Figure 7. Firing output of CA1 neurons along the longitudinal axis of hippocampus

A) Voltage traces showing trains of action potentials fired in response to depolarizing current injections in representative CA1 neurons from four regions of the ventral to dorsal (V–D) axis. **B-C)** Scatter plots of average firing frequency in response to 500 pA and 250 pA current injections with V–D position of individual neurons. Firing frequencies for both current intensities showed a strong negative correlation with V–D position (500 pA: r=-0.57, $P=3.8e^{-11}$; 250pA: r=-0.57, $P=2.18e^{-10}$). Black lines are linear fit and grey lines are segmented fits. **D-E)** Whisker and box plots showing the median and range of firing frequencies in response to 500 pA and 250pA current injections. Grey circles depict the mean values. Firing frequency for 500 pA current injection **(D)** was significantly different across the four bins of longitudinal axis (Kruskal-Wallis test, $P=4.4^{-11}$; Mann-Whitney U test for comparison among groups, $*P<0.005$, $**P<1e^{-5}$). Firing frequency for 250 pA current injection **(E)** was also significantly different across the four bins of longitudinal axis (Kruskal-Wallis test, $P=7.1^{-13}$; Mann-Whitney U test for comparison among groups, $*P<0.005$, $**P<1e^{-5}$). **F)** Scatter plot of spike frequency accommodation (SFA) index of CA1 neurons across the V-D axis. SFA index of CA1 neurons was positively correlated with the V–D position (r=0.53, $P<1e^{-9}$). SFA index was significantly different for neurons in

VHC (Kruskal-Wallis test, $P=3.75^{-7}$; Mann-Whitney U test for comparison among groups, $*P<0.018$).

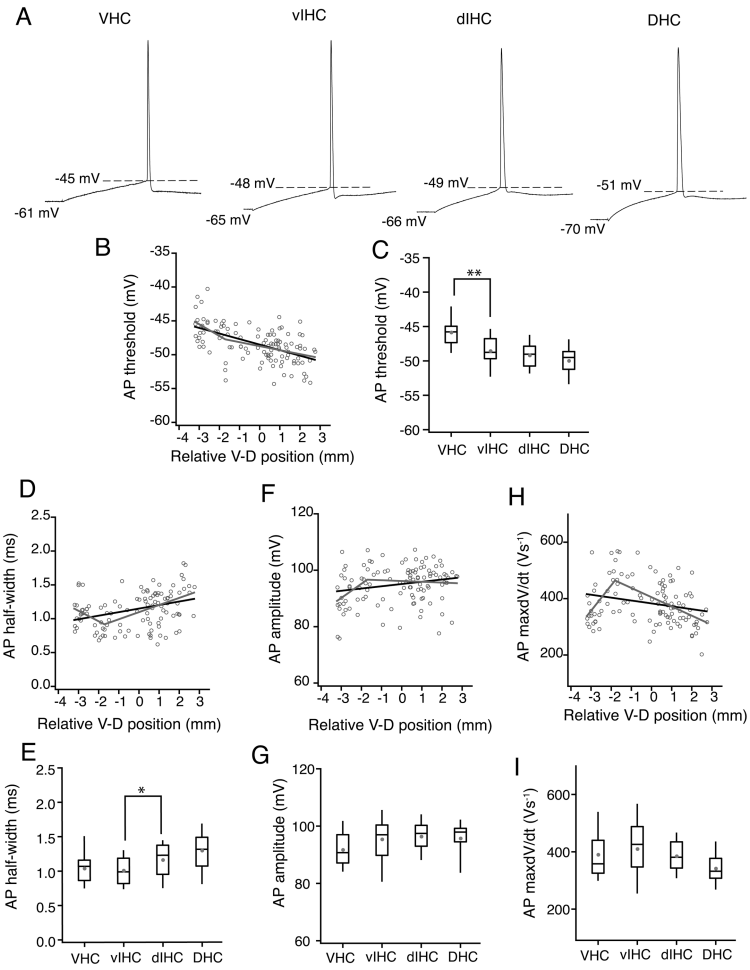

Figure 8. Single action potential properties of CA1 neurons along the longitudinal axis of hippocampus

A) Individual action potentials (AP) from representative CA1 neurons from four regions of the ventral to dorsal (V–D) axis. Dashed lines indicate the AP threshold. Voltage values in the bottom row indicate the RMP. **B, D, F and H)** Scatter plots for AP threshold **(B)**, AP half-width **(D)**, AP amplitude **(F)** and AP maximum dV/dt (H) of CA1 neurons against their relative V–D position. Black lines are the linear regression fits. Grey lines are segmented regressions fits. There was a significant negative correlation of AP threshold with V–D position ($r=-0.546$, $P=5.4e^{-10}$). AP half-width showed a slight positive correlation with V–D position ($r=0.34$, $P=2.1e^{-4}$). AP amplitude ($r=-0.2$, $P=0.02$) and AP max dV/dt ($r=-0.23$, $P=0.015$) were not significantly correlated with V-D position. **C, E, G and I)** Data are plotted as whisker and box plots showing the median values. Grey filled circles denote the mean values. AP threshold **(C)** was significantly depolarized for the neurons in VHC (Kruskal-Wallis test, $P=1.8^{-8}$; Mann-Whitney U test for comparison among groups, $^{**}P<1e^{-3}$). AP half-width **(E)** was significantly different between the neurons in dorsal half and ventral half of the hippocampus (Kruskal-Wallis test, $P=9^{-4}$; Mann-Whitney U test for comparison among groups, $^{*}P<0.019$). The difference across bins in AP amplitude **(G)**

(Kruskal-Wallis test, *P=0.03)* and AP max dV/dt **(I)** (Kruskal-Wallis test, *P=0.02*) was not significant.

Table 1

Linear regression model to predict the hippocampal slice position in longitudinal axis

Coefficients	Estimate	S.E.M.	*P* value
β_0	- 7.23	0.43	$1.2403e^{-39}$
β_1	0.43	0.02	$4.2266e^{-54}$
β_2	0.50	0.16	0.002
β_3	0.34	0.08	$9.3877e^{-05}$

Relative longitudinal position = $\beta_0 + \beta_1$(CA1 ratio) + β_2(DG ratio) + β_3(CA3 ratio). Number of observations: 207; Root Mean Squared Error: 0.55; R-squared: 0.93; Adjusted R-Squared 0.929.

Table 2

Regression parameters corresponding to linear and segmented fits for subthreshold electrophysiological properties of CA1 pyramidal neurons along the V–D axis

	Linear regression				Segmented regression								
										Breakpoint		Slopes comparison	
	Cons.	Slope	Adj. R^2	P-value	Cons.	Slope 1	Slope 2	Adj. R^2	P-value	Location	P-value	Diff.	P-value
RMP (mV)	-66.3	-1.55	0.68	<0.0001	-63.9	-0.58	-1.71	0.68	<0.0001	-1.99	0.033	1.12	0.12
R_{in} at RMP (MΩ)	59.6	-11.6	0.73	<0.0001	52.6	-15	-8.5	0.745	<0.0001	-0.53	0.526	-6.52	0.031
R_{in} at -65mV (MΩ)	66.2	-3.1	0.09	0.0007	49.1	-10.4	-0.7	0.115*	0.0005	-1.3	0.05	-9.74	0.05
Tau (ms)	23.9	-3.15	0.38	<0.0001	24.3	-1.9	-4	0.38	<0.0001	0.79	0.77	1.61	0.5

V–D gradients in subthreshold electrophysiological properties of CA1 pyramidal neurons were fitted by linear and segmented regressions. Linear regression had two factors: constant value (Cons.) and slope. Segmented regression had three factors: constant, slope of line one (slope 1) and slope of line two (slope 2). V–D change in a few electrophysiological properties fitted better with segmented regressions than linear regressions

*significant increase in Adjusted R^2

Table 3

Regression parameters corresponding to linear and segmented fit for morphological properties of CA1 pyramidal neurons along the V–D axis

	Linear regression				Segmented regression								
										Breakpoint		Slopes comparison	
	Cons.	Slope	Adj. R^2	P-value	Cons.	Slope 1	Slope 2	Adj. R^2	P-value	Location	P-value	Diff.	P-value
Total dendritic length (mm)	7.98	0.71	0.4	<0.0001	7.72	0.55	1.09	0.4	0.0004	0.6	0.82	-0.53	0.43
Apical radial length (mm)	0.73	-0.025	0.24	0.004	0.64	-0.07	0.013	0.42*	0.0003	-0.41	0.26	-0.08	0.005‡
Avg. number of intersections (proximal SR)	8.4	0.039	-0.03	0.86	22.3	5.1	-0.32	0.12*	0.05	-2.5	0.001†	5.4	0.02‡
Avg. number of intersections (distal SR)	10.1	1.6	0.46	<0.0001	13.9	3.4	0.64	0.54*	<0.0001	-0.93	0.3	2.8	0.02‡
Avg. number of intersections (SLM)	4.9	0.15	-0.014	0.44	4.3	-0.1	0.3	-0.04	0.66	-0.92	0.86	-0.4	0.6
Avg. number of intersections (basal)	9.28	1.78	0.75	<0.0001	10.05	2.2	1.3	0.76	<0.0001	-0.1	0.93	0.9	1.25

V–D gradients in morphological properties of CA1 pyramidal neurons were fitted by linear and segmented regressions. Linear regression had two factors: constant value (Cons.) and slope. Segmented regression had three factors: constant, slope of line one (slope 1) and slope of line two (slope 2). V–D change in a few electrophysiological properties fitted better with segmented regressions than linear regressions

*significant increase in Adjusted R^2;

†significant estimation of change point;

‡significant difference between the slopes of two lines in the segmented regression.

Table 4

Regression parameters corresponding to linear and segmented fits for I_h sensitive electrophysiological properties of CA1 pyramidal neurons along the V–D axis

	Linear regression				Segmented regression								
										Breakpoint		Slopes comparison	
	Cons.	Slope	Adj. R^2	P-value	Cons.	Slope 1	Slope 2	Adj. R^2	P-value	Location	P-value	Diff.	P-value
F_R at RMP (Hz)	3.14	-0.02	-0.01	0.57	3.5	0.14	-0.09	-0.001	0.39	-1.2	0.39	0.23	0.21
Q (RMP)	2.08	0.002	-0.01	0.73	1.19	-0.012	0.024	-0.005	0.49	0.5	0.7	-0.03	0.23
F_R at -65 mV (Hz)	3.06	-0.23	0.22	<0.0001	4.4	0.3	-0.3	0.23*	<0.0001	-2.1	0.006†	0.6	0.07
Q (-65 mV)	1.2	-0.03	0.15	<0.0001	1.18	-0.05	-0.009	0.155	<0.0001	0.09	0.946	-0.04	0.23
RS (at RMP)	-0.21	0.013	0.09	0.0007	-0.1	0.05	0.004	0.12*	0.0003	-1.8	0.017†	0.05	0.035‡
RS at -65mV	-0.22	0.028	0.29	<0.0001	-0.2	-0.038	-0.001	0.31*	0.0001	0.54	0.437	0.04	0.029‡

V–D gradient in I_h sensitive electrophysiological properties of CA1 pyramidal neurons was fitted by linear and segmented regressions. Linear regression had two factors: constant value (Cons.) and slope. Segmented regression had three factors: constant, slope of line one (slope 1) and slope of line two (slope 2). V–D change in a few electrophysiological properties fitted better with segmented regressions than linear regressions

*significant increase in Adjusted R^2;

†significant estimation of change point;

‡significant difference between the slopes of two lines in the segmented regression.

Table 5

Regression parameters corresponding to linear and segmented fit for firing properties of CA1 pyramidal neurons along the V–D axis

	Linear regression				Segmented regression								
										Breakpoint		Slopes comparison	
	Cons.	Slope	Adj. R^2	P-value	Cons.	Slope 1	Slope 2	Adj. R^2	P-value	Location	P-value	Diff.	P-value
AP threshold (mV)	-48.53	0.81	0.29	<0.0001	-50.7	-1.72	-0.58	0.3	<0.0001	-1.7	0.09	-1.13	0.1
AP hw (ms)	1.14	0.052	0.11	<0.0001	0.65	-0.15	0.1	0.18*	<0.0001	-2	0.0001†	-0.26	0.001‡
AP amplitude (mV)	95	0.079	0.035	0.0274	105.1	5	-0.3	0.08*	0.003	-1.7	0.002†	5.3	0.012
AP max dV/dt (mv/ms)	382.2	-10.2	0.05	0.012	625	-90.2	-32.7	0.25	0.0001	-1.8	0.0001	122.9	0.0001‡
Firing freq. (500 pA) (Hz)	26.5	-2.97	0.32	<0.0001	32.7	-0.01	-5.2	0.37*	<0.0001	-0.7	0.27	5.23	0.005‡
Firing freq. (250 pA) (Hz)	14.39	-3.74	0.47	<0.0001	19.4	-1.36	-5.72	0.49*	<0.0001	-0.633	0.376	4.35	0.011‡
SFA	2.23	0.2	0.26	<0.0001	2.3	0.24	0.17	0.25	<0.0001	-0.52	0.897	0.069	0.61

V–D gradient in firing properties of CA1 pyramidal neurons was fitted by linear and segmented regressions. Linear regression had two factors: constant value (Cons.) and slope. Segmented regression had three factors: constant, slope of line one (slope 1) and slope of line two (slope 2). V–D change in a few electrophysiological properties fitted better with segmented regressions than linear regressions

*significant increase in Adjusted R^2;

†significant estimation of change point;

‡significant difference between the slopes of two lines in the segmented regression.

Table 6
V–D gradients in electrophysiological and morphological properties of CA1 neurons

Neuronal property	V-D change	Linear/Segmented	Slope of linear fit (normalized to range)	Breakpoint location
RMP (mV)	Decrease	Linear	-0.09	n/a
R_{in} at RMP (MΩ)	Decrease	Linear	-0.1	n/a
R_{in} at -65mV (MΩ)	Decrease	Linear	-0.04	n/a
Tau (ms)	Decrease	Linear	-0.06	n/a
F_R at RMP (Hz)	No change	Linear	-0.007	n/a
Q (RMP)	No change	Linear	-0.003	n/a
F_R at -65 mV (Hz)	Decrease	Segmented	n/a	-2.1
Q (-65 mV)	Decrease	Linear	-0.04	n/a
RS (at RMP)	Decrease	Segmented	n/a	-1.8
RS at -65mV	Decrease	Segmented	n/a	0.54
AP threshold (mV)	Decrease	Linear	-0.06	n/a
AP hw (ms)	Decrease	Segmented	n/a	-2
AP amplitude (mV)	Decrease	Segmented	n/a	-1.7
AP max dV/dt (mv/ms)	Decrease	Segmented	n/a	-1.8
Firing freq. (500 pA) (Hz)	Decrease	Segmented	n/a	-0.7
Firing freq. (250 pA) (Hz)	Decrease	Segmented	n/a	-0.633
SFA	Increase	Linear	0.05	n/a
Total dendritic length (mm)	Increase	Linear	0.08	n/a
Apical radial length (mm)	Decrease	Segmented	n/a	-0.41
Number of intersections (proximal SR)	Increase	Segmented	n/a	0.5
Number of intersections (distal SR)	Increase	Segmented	n/a	-0.7
Number of intersections (SLM)	No change	Linear	0.01	n/a
Number of intersections (basal)	Increase	Linear	0.12	n/a

The slopes listed in this table were calculated by normalizing each dataset to its range (minimum and maximum). The slopes of the linear fits to the normalized values are listed in column three. Negative value of slopes corresponds to negative correlation (or decrease) of the neuronal property with ventral-to-dorsal location and positive values correspond to a positive correlation. Breakpoint locations are listed for the neuronal properties that showed segmented gradients along the longitudinal axis.